

# Charge-Symmetry Violation in Pion Scattering from Three-Body Nuclei

A. E. Kudryavtsev\* and V. E. Tarasov†

*Institute for Theoretical and Experimental Physics  
25 Bolshaya Cheremushkinskaya Street, Moscow 117259, Russia*

B. L. Berman‡, W. J. Briscoe§, K. S. Dhuga\*\*, and I. I. Strakovsky††

*Center for Nuclear Studies, Department of Physics  
The George Washington University, Washington, D.C. 20052  
(November 5, 2018)*

## Abstract

We discuss the experimental and theoretical status of charge-symmetry violation (CSV) in the elastic scattering of  $\pi^+$  and  $\pi^-$  on  ${}^3H$  and  ${}^3He$ . Analysis of the experimental data for the ratios  $r_1$ ,  $r_2$ , and  $R$  at  $T_\pi = 142, 180, 220,$  and  $256$  MeV provides evidence for the presence of CSV. We describe pion scattering from the three-nucleon system in terms of single- and double-scattering amplitudes. External and internal Coulomb interactions as well as the  $\Delta_{33}$ -mass splitting are taken into account as sources of CSV. Reasonable agreement between our theoretical calculations and the experimental data is obtained for  $T_\pi = 180, 220,$  and  $256$  MeV. For these energies, it is found that the  $\Delta_{33}$ -mass splitting and the internal Coulomb interaction are the most important contributions for CSV in the three-nucleon system. The CSV effects are rather sensitive to the choice of pion-nuclear scattering mechanisms, but at the same time, our theoretical predictions are much less sensitive to the choice of the nuclear wave function. It is found, however, that data for  $r_2$  and  $R$  at  $T_\pi = 142$  MeV do not agree with the predictions of our model,

---

\*kudryavt@heron.itep.ru

†tarasov@vitep5.itep.ru

‡berman@gwu.edu

§briscoe@gwu.edu

\*\*dhuga@gwu.edu

††igor@gwu.edu

which may indicate that there are additional mechanisms for CSV which are important only at lower energies.

PACS numbers: 25.45.De, 25.80.Dj, 24.80.+y, 25.10.+s

## I. INTRODUCTION

The issue of charge symmetry violation (CSV) is fundamental to our understanding of hadronic interactions, and many experimental and theoretical studies have addressed this issue (see review [1]). In the framework of QCD, CSV arises from the mass difference between the  $u$  and  $d$  quarks. The other principal cause for CSV comes from the electromagnetic interaction.

Weinberg [2] pointed out that the effective chiral  $\pi N$  Lagrangian, coming from QCD, contains a term which violates charge symmetry (see also, a recent review by Meissner [3]). Thus, not only are there kinematic reasons for CSV due to the mass differences within baryon multiplets, but direct CSV effects should exist as well. Recently, Gashi *et al.* [4] analyzed low-energy  $\pi N$  scattering data, and found some indications for direct CSV effects in the strong-interaction sector.

Another way to study CSV is through the pion-nuclear interaction in the lightest nuclei, particularly via isomirror elastic scattering. For the deuteron case, the  $\pi^+d$  cross section is compared with that for  $\pi^-d$  in Masterson *et al.* [5] and Baru *et al.* [6], but only small differences are found.

For pion elastic scattering from  ${}^3H$  and  ${}^3He$ , one can consider three mirror ratios formed from the differential cross sections:

$$\begin{aligned} r_1 &= \frac{d\sigma/d\Omega(\pi^+{}^3H)}{d\sigma/d\Omega(\pi^-{}^3He)}, \\ r_2 &= \frac{d\sigma/d\Omega(\pi^-{}^3H)}{d\sigma/d\Omega(\pi^+{}^3He)}, \text{ and} \\ R &= r_1 \cdot r_2, \end{aligned} \tag{1}$$

where  $R$  is referred to as the ‘‘superratio’’ [7]. The  $\pi^+{}^3H$  and  $\pi^-{}^3He$  scattering cross sections are isomirror ones, as are  $\pi^-{}^3H$  and  $\pi^+{}^3He$ . If charge symmetry were conserved, all three ratios would be equal to unity. Of course, the Coulomb interaction is not charge symmetric and has to be taken into account.

The experimental study of these ratios has been concentrated on large-angle scattering because the Coulomb interaction, which intrinsically violates charge symmetry, makes a significant contribution in the forward-scattering region. In a series of LAMPF experiments [7–10], the ratios (1) were measured in the range of the  $\Delta_{33}(1232)$   $\pi N$  resonance. Significant deviation (several standard deviations) from unity (up to  $\sim 20\%$ ) was observed for  $r_2$  and  $R$  in the angular range outside of the Coulomb cone,  $\theta \geq 30^\circ$ . In addition, strong angular dependence of both  $r_2$  and  $R$  was observed in the angular interval between  $\theta \simeq 60^\circ$  and  $90^\circ$ . These CSV effects are much more pronounced for  ${}^3H$  and  ${}^3He$  than for  ${}^2H$ , where the observed asymmetry  $A_\pi$ <sup>1</sup> is not nearly as large: it is only about 2% (see, for example,

---

<sup>1</sup>Historically, the CSV experimental data for  $\pi^\pm d$  elastic scattering have been evaluated in terms of the asymmetry  $A_\pi$ :

$$A_\pi = \frac{d\sigma/d\Omega(\pi^-d) - d\sigma/d\Omega(\pi^+d)}{d\sigma/d\Omega(\pi^-d) + d\sigma/d\Omega(\pi^+d)}.$$

Ref. [5]). In addition, inelastic-scattering data for the ratios (1) at excitation energy below 20 MeV have been reported in Ref. [11], and elastic differential cross sections at back angles in Ref. [12].

Thus, CSV effects manifest themselves clearly in the three-nucleon system, even if they are very small in the deuteron case. For this reason, the main goal of our theoretical analysis is the elucidation of the mechanisms that enhance CSV in the three-nucleon system. In other words, can the observed enhancement be due only to the well-known mass differences of the hadron multiplets together with the Coulomb interaction? Previous studies have indicated that the main reason for CSV in the case of the deuteron is the mass difference of the charge  $\Delta_{33}(1232)$ -isobar states. The influence of this effect on the scattering amplitude of the  $\pi d$  elastic scattering was discussed in the papers by Masterson *et al.* [5] and Baru *et al.* [6] for single and single-with-double scattering, respectively. Naturally, as the number of multiple-scattering diagrams increases with an increasing number of nucleons, one expects the effect of the  $\Delta_{33}$ -mass splitting to be more prominent for  ${}^3H$  and  ${}^3He$  than for  ${}^2H$ .

In addition to the interaction between charged pions and nuclei due to the external Coulomb force, there is an internal Coulomb interaction due to the difference in the wave functions (WFs) of  ${}^3H$  and  ${}^3He$ . (Note that in terms of the strong interaction, there is no difference between the WFs of  ${}^3H$  and  ${}^3He$ .) One difference in these WFs arises from the additional Coulomb repulsion between the two protons in  ${}^3He$ , which is not present in  ${}^3H$ .

In Ref. [13], the difference in the structure of  ${}^3H$  and  ${}^3He$  has been described by a first order optical potential in the pion-nuclear interaction in which the  ${}^3H$  and  ${}^3He$  charge and magnetic form factors extracted from experimental data on elastic electron scattering from  ${}^3H$  and  ${}^3He$  were used. A more detailed analysis of pion- ${}^3H/{}^3He$  elastic and inelastic scattering was reported in Ref. [14], where an optical single-scattering pion-nuclear potential, calculated at a microscopic level with a realistic three-nucleon wave function, was used. No reasonable description of the CSV effects was achieved when the calculations were performed with isospin-symmetric wave functions for both nuclei. A different approach was used in Ref. [15], where the difference in the WFs of  ${}^3H$  and  ${}^3He$  was taken into account explicitly. In all of these approaches [13–15], the difference in the structure of the three-nucleon system results in a sharp enhancement of the ratios  $r_2$  and  $R$  in the angular range  $60^\circ \leq \theta \leq 90^\circ$ .

One of the reasons for this behavior of the angular distribution is that the elastic differential cross section in the single-scattering approach contains a significant contribution at small scattering angles and has a minimum at  $\theta \simeq 90^\circ$  which is related to the dip in the  $\pi N$  non-spin-flip amplitude. Therefore, even a small contribution to the interaction that violates charge symmetry (*e.g.*, the Coulomb interaction) can produce an enhanced effect. The influence of the  $\Delta_{33}$ -mass splitting on the observed CSV effect might also result in a large effect in this angular range.

Moreover, to understand the angular distribution in detail, one must look beyond the

---

If we define  $r_d$  by analogy with the ratios (1), we get

$$r_d = \frac{d\sigma/d\Omega(\pi^-d)}{d\sigma/d\Omega(\pi^+d)} = 1 + \epsilon,$$

and for small  $\epsilon$  we have  $A_\pi = \epsilon/2$ . Thus,  $r_d \simeq 1 + 2A_\pi$ .

single-scattering approach to the  $\pi N$  interaction. We therefore examine the contributions of both single- and double- $\pi N$  scattering to the pion-nuclear scattering amplitude following techniques developed in Ref. [6]. We then take CSV effects into account to obtain expressions for the ratios (1), which then are compared with the experimental data [7–10].

An analysis of the experimental status for the ratios (1) at energies spanning the  $\Delta_{33}$  resonance is given in Section II. In Section III, we explain how the basic ingredients of the scattering amplitude and the constraints of single and double scattering are combined for  $\pi^3H$  and  $\pi^3He$  elastic scattering. In Section IV, we derive expressions for the scattering amplitudes, taking into account all three effects responsible for CSV. In Section V, we discuss the influence of these factors on the ratios (1) to show the effect of the individual CSV factors, and we compare the results of our calculations with the data. In Section VI, we discuss some related issues associated with CSV effects in other nuclei over broader ranges in energy and scattering angle. In Section VII, we summarize our findings.

## II. ANALYSIS OF THE EXPERIMENTAL STATUS

CSV in pion-nucleus scattering was first claimed to have been observed in the difference of total  $\pi^\pm d$  cross sections measured at PSI [16], and ascribed to the  $\Delta_{33}$ -mass splitting. Essentially, the total cross section is mainly determined by the forward scattering amplitude, which at small angles can be approximated well by single scattering. In this approach, the different charge states of the  $\Delta_{33}$  are excited in  $\pi^+$  and  $\pi^-$  scattering on the deuteron, and the result is the small observed CSV effect. This has been discussed widely (see *e.g.*, the book by Ericson and Weise [17]). The situation with the observation of CSV effects in the  $\pi^\pm d$  differential cross sections is less clear. The first systematic study of the CSV effect in the differential  $\pi^\pm d$  cross sections was done at LAMPF [5]. There have been several subsequent measurements at LAMPF and TRIUMF for both  $\pi^+d$  and  $\pi^-d$  (see Ref. [6] for details). The experimental data weakly suggest a small effect in the asymmetry  $A_\pi$  for the deuteron. For example, in Ref. [5], an asymmetry  $A_\pi \simeq 2\%$  at 143 MeV near  $90^\circ$  in the CM frame is reported. However, Smith *et al.* [18], in an independent measurement done at TRIUMF, reported asymmetries of  $-1.5 \pm 0.6\%$  at back angles and various energies. Thus, the magnitude of CSV is at most 1–2%, the sign is uncertain, and the experimental uncertainties are only slightly less than the  $A_\pi$  values themselves.

At about the same time, however, measurements of the ratios (1) for  ${}^3H$  and  ${}^3He$  at LAMPF obtained significantly larger effects. The first evidence for a sizable CSV in the differential  $\pi^\pm {}^3H/{}^3He$  cross sections <sup>2</sup> below and at the  $\Delta_{33}$  resonance was seen for the range of CM scattering angles between  $45^\circ$  and  $95^\circ$  [7]. The effect seems to peak near  $80^\circ$  in the CM frame (*e.g.*,  $r_2 \simeq R \simeq 1.2$  at 180 MeV [7]). The experiment was repeated with better statistics and systematics for approximately the same range of scattering angles at energies spanning the  $\Delta_{33}$  [8] and beyond [9]. These measurements also were extended to backward angles from  $120^\circ$  to  $170^\circ$  [19] and are reported in the previous paper [10]. The experimental

---

<sup>2</sup>To eliminate some of systematic uncertainties, normalized yields were used for the experimental determination of the ratios (1).

data for all three ratios (1) for incident pion energies between 142 and 256 MeV are shown in Fig. 1. The agreement between the four data sets, on the whole, is very good. The bump observed at  $\sim 80^\circ$ , corresponding to the minimum in the non-spin-flip amplitude, is obvious in the ratios  $r_2$  and  $R$  for 142 and 180 MeV (below and on the  $\Delta_{33}$  resonance). Thus, CSV effects in  $\pi^3H$  and  $\pi^3He$  scattering are large and statistically significant. The main goal of the present work is to provide a theoretical basis for these large effects in the three-nucleon system.

### III. AMPLITUDES OF PION ELASTIC SCATTERING FROM ${}^3H$ AND ${}^3He$

We formulate the pion-nuclear amplitude in the range of the  $\Delta_{33}$  resonance as a combination of a single- and double-scattering of pions from the nucleons in the nucleus. For the  $A = 3$  nuclei, the appropriate diagrams are shown in Fig. 2. The elementary  $\pi N$  amplitude  $\hat{f}_{\pi N}$  is taken as the  $P_{33}$  partial wave, as if  $\pi N$  scattering takes place entirely through the  $\Delta_{33}$  resonance:

$$\hat{f}_{\pi N} = f_{P_{33}} \cdot \hat{S} \cdot \hat{T}, \quad (2)$$

where

$$f_{P_{33}} = \frac{1}{2ik_{cm}} [e^{2i\delta_{33}(k)} - 1],$$

and  $\hat{S}$  and  $\hat{T}$  are the spin and isospin projection operators for the  $\pi N$  system for total spin 3/2 and isospin 3/2:

$$\hat{S} = 2(\hat{k}_1 \cdot \hat{k}_2) + i \vec{\sigma} \cdot [\hat{k}_1 \times \hat{k}_2] \text{ and } \hat{T} = \frac{1}{3}(2 + \vec{t} \cdot \vec{\tau}). \quad (3)$$

Here,  $\vec{t}$  and  $\vec{\tau}/2$  are the isospin operators of the pion and nucleon, respectively,  $\vec{\sigma}$  and  $\vec{\tau}$  are Pauli matrices,  $\hat{k}_1$  and  $\hat{k}_2$  are the unit vectors in the direction of the incoming and outgoing pions in CM frame, respectively, and  $\vec{k}_{cm}$  is the pion momentum in the CM frame. Everywhere below, we use the following notation:

$$\hat{S} = a + \hat{b}, \quad a = 2(\hat{k}_1 \cdot \hat{k}_2), \quad \hat{b} = (\vec{\sigma} \cdot \vec{b}), \text{ and } \vec{b} = i[\hat{k}_1 \times \hat{k}_2]. \quad (4)$$

The WF of the  ${}^3H$  and  ${}^3He$  can be written as

$$\Psi = \psi(\vec{r}_1, \vec{r}_2, \vec{r}_3) \sum_{i=1}^3 X_i \cdot Y_i, \quad (5)$$

where  $X_i$  and  $Y_i$  correspond to the spin and isospin parts of the WF, respectively:

$$X_i = \frac{1}{\sqrt{2}}(\chi_i^+ \chi) (\chi_j^+ \sigma_2 \chi_k^*) \text{ and } Y_i = \frac{1}{\sqrt{6}}(\eta_i^+ \vec{\tau} \eta) (\eta_j^+ \vec{\tau} \tau_2 \eta_k^*), \quad (6)$$

where  $\chi$  and  $\eta$  are the spinor and isospinor of the nucleus, respectively, and  $\chi_i$ ,  $\chi_j$ , and  $\chi_k$  ( $\eta_i$ ,  $\eta_j$ ,  $\eta_k$ ) are the spinors (isospinors) of the nucleons of the nucleus ( $i$ ,  $j$ , and  $k$  are cyclic).

Equations (6) represent states of pairs of nucleons ( $jk$ ) such that their total spin  $S = 0$  and their isospin  $T = 1$ . The representation (5) for the WFs of  ${}^3H$  and  ${}^3He$  can be generalized for more complicated wave configurations of nuclei, as is discussed in Ref. [20].

The coordinate part of the WF is taken into account in a symmetric form corresponding to a simple  $S$ -shell model. In the following calculations, we use two different forms of the radial WF:

i) The simple Gaussian form:

$$\psi(\vec{r}_1, \vec{r}_2, \vec{r}_3) \sim \exp\left[-\frac{1}{2b^2} \sum_{i=1}^3 (\vec{r}_i - \vec{R}_0)^2\right], \quad (7)$$

where  $b = 1.65 \text{ fm}$  and  $\vec{R}_0 = \frac{1}{3}(\vec{r}_1 + \vec{r}_2 + \vec{r}_3)$ , taken from Kamalov *et al.* [14]. The slope  $b = 1.65 \text{ fm}$  was chosen in Ref. [14] by a best fit to the experimental data for the  ${}^3H$  charge form factor below momentum transfer  $Q = 400 \text{ MeV}/c$  [21]. This form of the WF fails to reproduce the minimum of the charge form factor at  $Q \approx 710 \text{ MeV}/c$ ; however, the elastic  $\pi^\pm {}^3He$  differential cross sections are reproduced well at  $T_\pi = 100$  and  $200 \text{ MeV}$ , and at backward scattering angles, the results of the calculations with WF (7) tend toward the suppression seen in the experimental cross sections [14].

ii) The two-component Gaussian parametrization:

$$\psi(\vec{r}_1, \vec{r}_2, \vec{r}_3) = N \sum_{m=1}^2 D_m \exp\left[-\frac{\alpha_m}{2} \sum_{i=1}^3 (\vec{r}_i - \vec{R}_0)^2\right], \quad (8)$$

where  $D_1 = 1$ ,  $D_2 = -1.9$ ,  $\alpha_1 = 0.70 \text{ fm}^{-2}$ ,  $\alpha_2 = 2.24 \text{ fm}^{-2}$ , and  $N$  is a normalization constant given in Appendix A. This WF was successfully used by Foursat *et al.* [22] for the description of the differential cross sections for the reaction  ${}^4He(p, d){}^3He$  at  $770 \text{ MeV}$  for a wide range of scattering angles. The WF (8) reproduces the minimum of the  ${}^3He$  charge form factor at  $Q = 670 \text{ MeV}/c$ , but shows an enhancement at momentum transfer  $Q \approx 300 - 400 \text{ MeV}/c$ .

### A. Single-Scattering Approximation

The diagram in Fig. 2a corresponds to the single-scattering approximation for the elastic pion-nuclear scattering amplitude. To calculate this amplitude, we need to compute the matrix element for the operator (2) between initial- and final-state wave functions. We neglect both the Fermi motion of the nucleon inside the nucleus and the off-shell corrections to the  $\pi N$  amplitudes in expression (2). (We discuss the accuracy of both of these approximations in Sec. VIB.) Taking nuclear WFs in the form (5), we exclude spin and isospin variables of the nucleons. As in Ref. [20], the single-scattering amplitude  $\hat{F}_1$  is:

$$\hat{F}_1 = F(\vec{\Delta}) f_{P33} \hat{\Lambda}_1, \quad (9)$$

where  $F(\vec{\Delta})$  is a nuclear form factor defined by Eq. (A4) and  $\vec{\Delta}$  is the three-momentum transfer. The operator  $\hat{\Lambda}_1$  acts on the nuclear spin and isospin variables and is expressed as

$$\hat{\Lambda}_1 = \frac{1}{3}[(6 + \vec{t} \cdot \vec{\tau}) a + (2 - \vec{t} \cdot \vec{\tau}) \hat{b}], \quad (10)$$

where  $a$  and  $\hat{b}$  have been defined in Eq. (4). Calculating the matrix element from the operator  $\hat{\Lambda}_1$  on isotopic variables, we get

$$\hat{\Lambda}_1 = \begin{cases} \frac{1}{3}(7 a + \hat{b}) & \text{for } \pi^{+3}He \text{ and } \pi^{-3}H \text{ scattering,} \\ \frac{1}{3}(5 a + 3 \hat{b}) & \text{for } \pi^{+3}H \text{ and } \pi^{-3}He \text{ scattering.} \end{cases} \quad (11)$$

In terms of  $\hat{\Lambda}_1$ , the expression for the differential cross section with unpolarized particles yields:

$$\frac{d\sigma}{d\Omega} = F^2(\vec{\Delta}) |f_{P_{33}}(k)|^2 \frac{1}{2} Tr\{\hat{\Lambda}_1^+ \hat{\Lambda}_1\}, \quad (12)$$

where

$$\frac{1}{2} Tr\{\hat{\Lambda}_1^+ \hat{\Lambda}_1\} = \begin{cases} \frac{1}{9}(1 + 195 z^2) & \text{for } \pi^{+3}He \text{ and } \pi^{-3}H \text{ scattering,} \\ \frac{1}{9}(9 + 91 z^2) & \text{for } \pi^{+3}H \text{ and } \pi^{-3}He \text{ scattering,} \end{cases} \quad (13)$$

where  $z = (\vec{k}_1 \cdot \vec{k}_2) = \cos \theta$ . In addition to a lower form factor  $F(\vec{\Delta})$ , the angular dependence of  $d\sigma/d\Omega$  is determined by the factors of Eq. (13). Expressions (12) and (13) show that  $d\sigma/d\Omega$  is suppressed at  $z = 0$  ( $\theta = 90^\circ$ ), where only the spin-flip  $\pi N$  amplitude contributes. Thus, for the  $A = 3$  case, there is a more significant spin-flip suppression than for the deuteron case, where (see, for example, Ref. [6])

$$\frac{d\sigma_{\pi d}}{d\Omega} \sim (1 + 5 z^2)$$

and the minimum in the cross section is much weaker. We note that this kind of suppression of the spin-flip  $\pi N$  amplitude in the single-scattering term for the  ${}^3H/{}^3He$  case was pointed out in Ref. [7], following Ref. [23].

In Figs. 3 – 6, the single-scattering contributions to the differential cross sections for incident pion kinetic energies  $T_\pi = 142, 180, 220,$  and  $256$  MeV, for both versions of the radial part of the WFs (7) and (8), are shown by the dashed curves.

## B. Double-Scattering Approximation

Let us consider the double-scattering amplitude  $\hat{F}_2$ , as in Ref. [20], corresponding to the diagram shown in Fig. 2b. (Calculations of double-spin-flip amplitudes were performed recently [24].) In the same approximation as was used while calculating the single-scattering term,

$$\hat{F}_2 = 4\pi \frac{9}{2} f_{P_{33}}^2 \int \frac{d^3 \vec{q}}{(2\pi)^3} \frac{d^3 \vec{Q}}{(2\pi)^3} \frac{d^3 \vec{Q}'}{(2\pi)^3} \varphi(\vec{q}, \vec{Q}') \varphi(\vec{q}, \vec{Q}) G_\pi \hat{\Lambda}_2, \quad (14)$$

where the WF in the momentum space operator  $\varphi(\vec{q}, \vec{Q})$  is defined by Eq. (A2). The momenta  $\vec{q}, \vec{Q}, \vec{Q}'$ , and  $\vec{q}'$  relate to the momenta  $\vec{p}_i$  and  $\vec{p}'_i$ , shown in Fig. 2b, via  $\vec{q} = (\vec{p}_2 - \vec{p}_3)/2$ ,



$\vec{Q} = (\vec{p}_2 + \vec{p}_3 - \vec{p}_1)/3$ ,  $\vec{Q}' = (\vec{p}'_2 + \vec{p}'_3 - \vec{p}'_1)/3$ , and  $\vec{q}' = \vec{q} - \frac{1}{2}\vec{Q} + \frac{1}{2}\vec{Q}' + \frac{1}{3}\vec{\Delta}$ . In Eq. (14),  $G_\pi$  is the Green's function for the intermediate state, which, neglecting kinetic energy of the intermediate nucleons, has the form

$$G_\pi = (k_1^2 - \vec{s}^2 + i0)^{-1}, \quad (15)$$

where  $\vec{s} = \vec{k}_1 - \vec{Q} + \vec{Q}' - \frac{1}{3}\vec{\Delta}$ . By analogy with Eq. (4), we introduce  $a_i$  and  $\hat{b}_i$ , where  $i = 1, 2$ , for the first and second nucleons:

$$a_{1,2} = 2 (\hat{k}_{1,2} \cdot \hat{s}) \text{ and } \hat{b}_{1,2} = (\vec{\sigma} \cdot \vec{b}_{1,2}), \quad (16)$$

where  $\vec{b}_1 = i [\hat{k}_1 \times \hat{s}]$ ,  $\vec{b}_2 = i [\hat{s} \times \hat{k}_2]$ , and  $\hat{s} = \vec{s}/|\vec{s}|$ . The operator  $\hat{\Lambda}_2$  then can be written as

$$\hat{\Lambda}_2 = \frac{4}{9}(5 + \vec{t} \cdot \vec{\tau})a_1a_2 + \frac{4}{9}(a_1\hat{b}_2 + a_2\hat{b}_1) - \frac{1}{9}(6 + 3\vec{t} \cdot \vec{\tau})\hat{b}_1\hat{b}_2 - \frac{1}{9}(6 + 5\vec{t} \cdot \vec{\tau})\hat{b}_2\hat{b}_1. \quad (17)$$

The operator  $\hat{\Lambda}_2$  depends explicitly on the spin and isospin variables of the nuclei and the pion.  $\hat{\Lambda}_2$  also depends on the vector  $\hat{s}$ , which is an integrative variable on the right-hand side of Eq. (14). We extract  $\hat{s}$  by introducing the operators  $\hat{\Lambda}_{2,ij}$ :

$$\hat{\Lambda}_2 = \sum_{i,j} \Lambda_{2,ij} \hat{s}_i \hat{s}_j. \quad (18)$$

Thus, the operator  $\hat{F}_2$  can be expressed in the form

$$\hat{F}_2 = \sum_{i,j} f_{P_{33}}^2 \Lambda_{2,ij} I_{ij}, \quad (19)$$

where the tensor  $I_{ij}$  is expressed in the form

$$I_{ij} = J_1 \hat{k}_i \hat{k}_j + J_2 \delta_{ij}, \quad (20)$$

such that  $\vec{\kappa} = (\vec{k}_1 + \vec{k}_2)/2$  and  $\hat{\kappa} = \vec{\kappa}/|\vec{\kappa}|$ . Here, the quantities  $J_1$  and  $J_2$  are complex functions which depend on the momentum of the incoming pion  $k_1$  and the momentum transfer  $\Delta$  (or on the scattering angle  $\theta$ ). They also depend on the WFs of the nuclei, which are given in Appendix B. Using Eq. (20) for the tensors  $I_{ij}$ , the amplitude  $\hat{F}_2$  becomes

$$\hat{F}_2 = A_2 + i B_2 (\vec{\sigma} \cdot [\hat{k}_1 \times \hat{k}_2]). \quad (21)$$

We divide the contributions to  $A_2$  and  $B_2$  into double elastic scattering

$$\pi^- \rightarrow \pi^- \rightarrow \pi^-$$

(we will define this contribution via index “ $ee$ ”) and double charge exchange

$$\pi^- \rightarrow \pi^0 \rightarrow \pi^-$$

(we will denote this contribution via index “ $cc$ ”) in the functions  $A_2$  and  $B_2$ :

$$A_2 = A_2^{ee} + A_2^{cc} \text{ and } B_2 = B_2^{ee} + B_2^{cc}. \quad (22)$$

Then, we can present expressions for  $A_2$  and  $B_2$  in terms of the integrals  $J_1$  and  $J_2$ :

$$\begin{aligned}
A_2^{cc} &= -\frac{1}{9}f_{P_{33}}^2[(3+5z)J_1 + 12zJ_2], & B_2^{ee} &= \frac{4}{3}f_{P_{33}}^2(J_1 + 2J_2), \\
A_2^{ee} &= \frac{1}{3}f_{P_{33}}^2[(23+17z)J_1 + 28zJ_2], & B_2^{cc} &= -\frac{2}{9}f_{P_{33}}^2(2J_1 + 3J_2) \text{ for } \pi^{+3}\text{He}, \pi^{-3}\text{H}, \\
A_2^{ee} &= \frac{1}{9}f_{P_{33}}^2[(29+27z)J_1 + 52zJ_2], & B_2^{cc} &= -\frac{2}{9}f_{P_{33}}^2(2J_1 + 5J_2) \text{ for } \pi^{-3}\text{He}, \pi^{+3}\text{H}. \quad (23)
\end{aligned}$$

The resulting double-scattering contributions to the differential cross sections are shown by the dotted curves in Figs. 3 – 6.

### C. Nonresonant Contributions

Although, the  $\pi N$   $P$ -wave amplitude is dominant for the multiple scattering of pions on the nucleons of nucleus in the energy range under consideration, the contribution of small nonresonant waves still can play an important role near  $\theta \sim 90^\circ$  (the sharp minimum for single scattering). Thus, we limit ourselves to single scattering for nonresonant waves. In this limit, the  $\pi N$  amplitude (2) becomes

$$\hat{f}_{\pi N} = \sum_j f_j \cdot \hat{S}_j \cdot \hat{T}_j, \quad (24)$$

where

$$f_j = \frac{1}{2ik_{cm}} [e^{2i\delta_j(k)} - 1]$$

and  $\hat{S}_j$  and  $\hat{T}_j$  are the spin and isospin projection operators for the state  $j$  of the  $\pi N$  system. Limiting ourselves to  $S$ - and  $P$ -waves, the nonresonant  $\pi N$   $\delta_j(k)$  phases can be taken from a recent GW  $\pi N$  partial-wave analysis [25]. Therefore, we take into account two  $S$ - and four  $P$ -waves in our calculations. The projection operators are

$$\begin{aligned}
\hat{S}_j &= \hat{1} & (S_{11}, S_{31}), \\
\hat{S}_j &= z - i(\vec{\sigma} \cdot \vec{n}) & (P_{11}, P_{31}), \\
\hat{S}_j &= 2z + i(\vec{\sigma} \cdot \vec{n}) & (P_{13}, P_{33}), \\
\hat{T}_j &= \frac{1}{3}(1 - \vec{t} \cdot \vec{\tau}) & (S_{11}, P_{11}, P_{13}), \text{ and} \\
\hat{T}_j &= \frac{1}{3}(2 + \vec{t} \cdot \vec{\tau}) & (S_{31}, P_{31}, P_{33}), \quad (25)
\end{aligned}$$

where  $\vec{n} = [\hat{k}_1 \times \hat{k}_2]$ . We note that the procedure of taking into account nonresonant waves in the single-scattering approach is analogous to the resonant contribution taken into account and discussed in Sec. III A. The final expressions for the non-spin-flip and spin-flip nonresonant amplitudes are

$$\begin{aligned}
A_{non} &= \left[ \frac{2}{3}f_{S_{11}} + \frac{7}{3}f_{S_{31}} + \left( \frac{2}{3}f_{P_{11}} + \frac{7}{3}f_{P_{31}} + \frac{4}{3}f_{P_{13}} \right) z \right] F(\Delta) \text{ and} \\
B_{non} &= \frac{1}{3}(2f_{P_{13}} - f_{P_{31}} - 2f_{P_{11}}) F(\Delta) \text{ for } \pi^{+3}\text{He} \text{ and } \pi^{-3}\text{H}, \text{ and}
\end{aligned}$$

$$\begin{aligned}
A_{non} &= \left[ \frac{4}{3}f_{S_{11}} + \frac{5}{3}f_{S_{31}} + \left( \frac{4}{3}f_{P_{11}} + \frac{5}{3}f_{P_{31}} + \frac{8}{3}f_{P_{13}} \right) z \right] F(\Delta) \quad \text{and} \\
B_{non} &= -f_{P_{31}} F(\Delta) \quad \text{for } \pi^- {}^3\text{He} \text{ and } \pi^+ {}^3\text{H}.
\end{aligned}
\tag{26}$$

The nonresonant contribution for the total amplitude  $\hat{F} = \hat{F}_1 + \hat{F}_2$  (see Eq. (27) below) is expressed by the substitutions

$$A \rightarrow A + A_{non} \text{ and } B \rightarrow B + B_{non}.$$

The nonresonant amplitudes are taken into account in the calculations of the ratios (1) presented in Sec. V.

#### D. Total Amplitude and Differential Cross Section

The expression for the sum of the single- and double-scattering amplitudes can be expressed in a form similar to Eq. (21):

$$\hat{F} = A + i B (\vec{\sigma} \cdot [\hat{k}_1 \times \hat{k}_2]), \tag{27}$$

where the functions  $A$  and  $B$  represent the contributions of single and double scattering, *e.g.*,  $A = A_1 + A_2$  and  $B = B_1 + B_2$ . The amplitudes  $A_1$  and  $B_1$  are determined by Eqs. (9) – (11) and (26);  $A_2$  and  $B_2$  by Eqs. (22) – (23). In terms of the functions  $A$  and  $B$ , the differential cross section in unpolarized case has the form

$$\frac{d\sigma}{d\Omega} = \frac{1}{2} Tr\{\hat{F}^+ \hat{F}\} = |A|^2 + |B|^2 \sin^2 \theta. \tag{28}$$

The combined single- and double-scattering contributions, with interference taken into account, are depicted by the solid curves in Figs. 3 – 6. It can be seen that the model approach we use qualitatively agrees with the data. For forward scattering,  $\theta \sim 30 - 60^\circ$ , WF (7) reproduces the cross sections systematically better than WF (8). At larger scattering angles, the results for WF (7) (WF (8)) lie below (above) the experimental data, and the cross-section minimum is shifted to a smaller angle ( $\theta \sim 80^\circ$ ), in agreement with the experimental data. The key point to be made, however, is that the gentle maximum at  $\theta \sim 110 - 120^\circ$  arises from the interference between single and double scattering. It is also seen that the moderation of the rise in the cross sections for backward scattering reflects the contribution of double scattering, which is most pronounced near  $\theta \sim 180^\circ$ .

We point out that the description of hadron-nuclear scattering in the backward hemisphere is a very complicated many-body problem that requires detailed information about the wave function of the nucleus and the reaction mechanism. For example, the 5-component WF used in Ref. [14] to describe the  $\pi^\pm {}^3\text{He}$  elastic cross sections at  $T_\pi = 200$  MeV is superior to WF (7). However, the goal of our study is the description and understanding of CSV effects, and these effects do not depend strongly on the details of the WF at small distances. For this reason, we prefer to use the simpler  $S$ -shell versions of the nuclear WFs (7) and (8).

## IV. CHARGE-SYMMETRY VIOLATION EFFECTS

There are three principal sources of the violation of charge symmetry for  $\pi^\pm$  scattering from light nuclei in the  $\Delta_{33}$  region:

1. the Coulomb interaction between the charged pions and the nuclei – the external Coulomb effect,
2. the mass splitting of the different charge states of the  $\Delta_{33}$ -isobar, and
3. the difference between the WFs of  ${}^3H$  and  ${}^3He$  due to the additional Coulomb repulsion between the two protons in the  ${}^3He$  nucleus – the internal Coulomb effect.

We now discuss how we take these effects into account in our calculation of the elastic scattering of charged pions from the  $A = 3$  nuclei.

### A. External Coulomb Effect

As was shown in Sec. II, experimental data for the ratios (1) [7–10] were taken outside the Coulomb cone,  $\theta \geq 30^\circ$ . In this angular range, the Coulomb amplitude is a smooth function of the scattering angle  $\theta$ . Here, we take into account the Coulomb interaction in a nonrelativistic approach, neglecting the interaction between the photon and the magnetic moment of the nucleus. Thus, the Coulomb amplitude of the pion-nucleus interaction in terms of the Coulomb phase may be written as

$$A_C = -\frac{Z_\pi Z_A e^2}{2k_{cm}^2 \sin^2 \frac{\theta}{2}} \frac{\omega m_A}{m_A + \omega} \exp\left[-\frac{2iZ_\pi Z_A e^2}{k_{cm}} \frac{\omega m_A}{m_A + \omega} \ln\left(\sin \frac{\theta}{2}\right)\right] F_\pi(\vec{\Delta}) F(\vec{\Delta}), \quad (29)$$

where  $e^2 \simeq 1/137$ ,  $Z_\pi$  and  $Z_A$  are the charges of the pion and the nucleus, respectively,  $\omega$  is the pion CM energy,  $m_A$  is the mass of the nucleus,  $F(\vec{\Delta})$  is the form factor of the nucleus defined by the Eq. (A4), and  $F_\pi(\vec{\Delta})$  is the pion charge form factor that is used in the standard parametrization of Ref. [26]. In calculating the ratios (1), we use the amplitude  $A_C$  of Eq. (29) in combination with the non-spin-flip amplitude  $A$  of the strong interaction of Eq. (27) by the substitution  $A \rightarrow A + A_C$ .

### B. $\Delta_{33}(1232)$ -Mass Splitting

The influence of the  $\Delta_{33}$ -mass splitting on the differential cross section for  $\pi d$  elastic scattering was discussed in Ref. [5], where the single-scattering approximation with allowance for the different charge states of the  $\Delta_{33}(1232)$  was used. In this approximation, the CSV effect proves to be independent of the scattering angle, with a value proportional to  $\delta m_\Delta / \Gamma_\Delta$ . Nearly the same approach was used for the  ${}^3H/{}^3He$  case in Ref. [7].

We denote the different charge states of the  $\Delta_{33}$  via the index  $i = 1, 2, 3$ , and 4 for the  $\Delta^{++}$ ,  $\Delta^+$ ,  $\Delta^0$ , and  $\Delta^-$ , respectively. The mass  $w_i$  ( $i = 1, 2, 3, 4$ ), corresponding to the isobar  $i$ , is calculated according to a formula from Ref. [17] (page 109, Eq. (4.18)), following Ref. [27]:

$$w_i = a - b I_i + c I_i^2, \quad (30)$$

where  $I_i$  is the  $3^{rd}$  component of isospin for the  $i^{th}$ -term from the  $\Delta_{33}$ -multiplet. Using the average resonance mass value from the Particle Data Group [28],  $\bar{w} = 1232 \text{ MeV}$ ,  $b = 1.38 \text{ MeV}$  from Ref. [17], and

$$w_3 - w_1 = m_{\Delta^0} - m_{\Delta^{++}} \simeq 2.5 \text{ MeV}$$

from Ref. [28], we get

$$a \simeq 1231.8 \text{ MeV} \text{ and } c = 0.13 \text{ MeV}.$$

The scalar amplitude for  $\pi N$  scattering (see Eq. (2)) for each charge state  $i$  is defined as

$$f_{P_{33}} \rightarrow f_i = \frac{1}{2ik_{cm}} [e^{2i\delta_i(k)} - 1]. \quad (31)$$

The phases  $\delta_i$  are defined relative to the resonance phase  $\delta_{P_{33}}$

$$\delta_i = \delta_{P_{33}} - 2 \frac{\delta w_i}{\Gamma_{\Delta}} \sin^2 \delta_{P_{33}}, \quad (32)$$

where  $\delta w_i = w_i - \bar{w}$ . The resonance phase  $\delta_{P_{33}}$  is taken from [25]. In Eq. (32), we neglect the energy dependence of the width  $\Gamma_{\Delta}$  because  $\delta w_i / \Gamma_{\Delta} \ll 1$ ; in our calculations we use  $\Gamma_{\Delta} = 120 \text{ MeV}$ . Using this definition of  $f_i$  for the  $\pi N$  scattering amplitudes in Eq. (31), we obtain the following expressions for the single pion-nucleus scattering amplitudes:

$$A_1 = (2f_1 + \frac{1}{3}f_2)2zF(\vec{\Delta}) \text{ and } B_1 = \frac{1}{3}f_2F(\vec{\Delta}) \text{ for } \pi^{+3}\text{He} \text{ and} \quad (33)$$

$$A_1 = (f_1 + \frac{2}{3}f_2)2zF(\vec{\Delta}) \text{ and } B_1 = f_1F(\vec{\Delta}) \text{ for } \pi^{+3}\text{H}. \quad (34)$$

Substituting  $f_1 \rightarrow f_4$  and  $f_2 \rightarrow f_3$ , the amplitudes  $A_1$  and  $B_1$  at Eqs. (33) and (34) are transformed to the amplitudes for the isomirror reactions  $\pi^{-3}H$  and  $\pi^{-3}He$ .

For the double-scattering pion-nucleus amplitudes, we obtain

$$A_2^{cc} = -\frac{1}{9}f_2^2[(3+5z)J_1 + 12zJ_2] \text{ and } B_2^{ee} = \frac{4}{3}f_1f_2(J_1 + 2J_2) \text{ for } \pi^{+3}\text{He}, \pi^{+3}\text{H} \quad (35)$$

instead of Eq. (23). The other amplitudes for  $\pi^{+3}He$  and  $\pi^{+3}H$  elastic scattering are different:

$$\begin{aligned} A_2^{ee} &= \frac{4}{3}f_1f_2[2(1+z)J_1 + 4zJ_2] + f_1^2[(5+3z)J_1 + 4zJ_2] & \text{for } \pi^{+3}He, \\ A_2^{ee} &= \frac{4}{3}f_1f_2[2(1+z)J_1 + 4zJ_2] + \frac{1}{9}f_2^2[(5+3z)J_1 + 4zJ_2] & \text{for } \pi^{+3}H, \\ B_2^{cc} &= -\frac{2}{9}f_2^2(2J_1 + 3J_2) & \text{for } \pi^{+3}He, \text{ and} \\ B_2^{cc} &= -\frac{2}{3}f_2^2(2J_1 + 5J_2) & \text{for } \pi^{+3}H. \end{aligned} \quad (36)$$

The amplitudes  $A_2$  and  $B_2$  of Eqs. (35) and (36) are also transformed to their isomirror reaction amplitudes, *i.e.*,  $\pi^{+3}He \rightarrow \pi^{-3}H$  and  $\pi^{+3}H \rightarrow \pi^{-3}He$ , by substituting  $f_1 \rightarrow f_4$  and  $f_2 \rightarrow f_3$ . We do not include any difference for the different charge states in the nonresonant amplitudes  $A_{non}$  and  $B_{non}$ .

### C. Internal Coulomb Effect

The difference in the structure of the WFs of  ${}^3H$  and  ${}^3He$  is related not only to the electromagnetic interaction, but also to the the part of the strong interaction which violates isospin. In the strong-interaction sector, there are terms that violate isospin directly [2]. Isospin violation inside nuclei can relate to both nucleon and quark degrees of freedom. In terms of quark degrees of freedom, isospin violation relates to the mass difference of the  $u$  and  $d$  quarks. At present, there is no quantitatively good estimate of isospin violation due to the strong interaction for the  $A = 3$  nuclei.

If we assume that the strong interaction conserves isospin, then the main reason for the difference in the structure of the WFs of  ${}^3H$  and  ${}^3He$  is the additional Coulomb repulsion between the two protons in  ${}^3He$ , which is not present for  ${}^3H$ .

If there were no Coulomb interaction between these two protons (*i.e.*, if the WFs of  ${}^3H$  and  ${}^3He$  were isotopically symmetric), the neutron distribution for  ${}^3He$  (the “odd” neutron) would be the same as the proton distribution for  ${}^3H$  (the “odd” proton), and the proton distribution for  ${}^3He$  (the “even” protons) would be the same as the neutron distribution for  ${}^3H$  (the “even” neutrons). However, the proton distributions for  ${}^3H$  and  ${}^3He$  can still be different and, as a consequence, so can the charge form factors of  ${}^3H$  and  ${}^3He$ .

If, however, isospin is violated for  ${}^3H$  and  ${}^3He$ , the even- and odd-nucleon distributions can also be different. In Ref. [15], the difference between these distributions has been formulated in terms of nonzero parameters  $\delta_e$  and  $\delta_o$ , where

$$\delta_e = r_e^n - r_e^p \text{ and } \delta_o = r_o^n - r_o^p.$$

Here,  $r_{e,o}^{n,p}$  is the neutron (n) or proton (p) radius for the even (e) or odd (o) nucleons. As was shown in Ref. [15], the superratio  $R$  at  $T_\pi = 180 \text{ MeV}$  is very sensitive to  $\delta_e$  and  $\delta_o$ ; a reasonable description of  $R$  versus scattering angle has been obtained for  $\delta_e = -0.030 \pm 0.008 \text{ fm}$  and  $\delta_o = 0.035 \pm 0.007 \text{ fm}$ . These differences between  $r_e^n$  and  $r_e^p$  or between  $r_o^n$  and  $r_o^p$  due to isospin violation result in additional changes in the charge radii and form factors of  ${}^3H$  and  ${}^3He$ .

We vary the parameters of the WFs (7) and (8) to introduce such differences. For WF (7), we follow the recipe suggested in Ref. [14]: we fix the slope  $b$  for  ${}^3H$  at  $1.65 \text{ fm}$  and vary the slope for  ${}^3He$  to obtain the best description of the data for the ratios  $r_1$  and  $r_2$ . An analogous procedure is followed for WF (8), using parameters for the WF for  ${}^3He$  suggested in Ref. [22] (see Sec. III). Then, for the WF of  ${}^3H$ , we use three different variations of the WF: (i) a variation of the slope  $\alpha_1$ , (ii) a variation of the slope  $\alpha_2$ , and (iii) a variation of both slopes  $\alpha_1$  and  $\alpha_2$ , which are proportional to each other:  $\alpha_1 \rightarrow c\alpha_1$  and  $\alpha_2 \rightarrow c\alpha_2$ .

Although this variation of the parameters of WFs (7) and (8) cannot be compared directly with the refined procedure used in Ref. [15], this way of taking into account the internal Coulomb interaction allows us to take the the  $\Delta_{33}(1232)$ -mass splitting into account, which was not done in Ref. [15]. Therefore, the quantities  $\delta_e$  and  $\delta_o$  obtained from the experimental data can differ from the values obtained in Ref. [15].

## V. COMPARISON WITH THE EXPERIMENTAL DATA

### A. Excluding the Internal Coulomb Effect

The results of our calculations for the ratios  $r_1$ ,  $r_2$ , and the superratio  $R$  which take into account the external Coulomb interaction and the  $\Delta_{33}$ -mass splitting but exclude the internal Coulomb effect are shown in Figs. 7 – 10, as the dotted curves for single scattering and the dashed curves for both single and double scattering. There are no free parameters associated with these results. The main purpose of Figs. 7 – 10 (as for Figs. 3 – 6) is to show that the inclusion of double scattering is essential to be able to follow the trend of the data in the non-spin-flip-dip region. As is seen in these figures, there is qualitative agreement between the results of our calculations and the data for  $T_\pi = 180, 220,$  and  $256$  MeV. Also, in contrast with the case for the differential cross section (see Figs. 3 – 6), there is little sensitivity to the WF here. For  $T_\pi = 180$  MeV, the ratio  $r_1$  is reproduced very well for both WFs (7) and (8), but the peaks near  $\theta = 80^\circ$  in the ratio  $r_2$  and superratio  $R$  are reproduced better by WF (7). At the same time, the description of  $r_2$  and  $R$  in the backward direction is not good for either WF. Figure 8 shows that even taking into account single scattering and the external Coulomb interaction cannot reproduce the experimental data there. But overall, Figs. 8 – 10 show that taking into account the  $\Delta_{33}$ -mass splitting consistently with both the single- and double-scattering contributions reproduces the main structures of the angular distribution and that we do not require a detailed knowledge of the nuclear WF.

We note here that the data for  $r_2$  and  $R$  for  $T_\pi = 142$  MeV are not reproduced by our model approach. Apparently, some other mechanism must play a role at this energy. We return to this problem below.

### B. Including the Internal Coulomb Effect

We now describe the CSV effects by taking into account the internal Coulomb interaction as well. The procedure for variation of the WFs is described above. For this case, we vary a single free parameter to obtain the best fit. Again, we fit  $r_1$  and  $r_2$  only, since the superratio  $R (= r_1 \cdot r_2)$  is not an independent quantity. The best-fit results for this approach and for both WFs (7) and (8) are shown in Figs. 11 – 14 by the solid curves. By comparison, the results without the internal Coulomb interaction (from Figs. 7 – 10) are shown by the dashed curves. Both free parameters  $\alpha_1$  and  $\alpha_2$  have been varied simultaneously, following our prescription (iii) of Sec. IV. The results of varying either  $\alpha_1$  or  $\alpha_2$  independently are very similar, as listed in the Table. In this Table, the best-fit results obtained by variations of the radii of the nuclei and corresponding  $\chi^2$  values are listed as well.

In Fig. 12, we see that our calculations reproduce all the ratios  $r_1$ ,  $r_2$ , and  $R$  for  $T_\pi = 180$  MeV rather well over the entire angular range. In fact, we reproduce the superratio  $R$  for  $40^\circ \leq \theta \leq 110^\circ$  much as Gibbs and Gibson did [15]. Taking into account the difference in the WFs of  ${}^3H$  and  ${}^3He$  results in a much better reproduction both of the quantity  $R$  at  $\theta \sim 80^\circ$  and the scattering at backward angles. Thus, taking into account the internal Coulomb interaction provides a substantial improvement in  $\chi^2$  compared with the case where only the external Coulomb interaction and the  $\Delta_{33}$ -mass splitting are included.

Finally, we consider the description of the data for  $T_\pi = 220$  and  $256$  MeV to be qualitatively satisfactory, while the description of the data for  $T_\pi = 142$  MeV is not. Consider the situation for  $T_\pi = 220$  MeV, shown in Fig. 13. Our theoretical curves reproduce the sharp

dip-bump angular dependence of the ratios  $r_2$  and  $R$  remarkably well. At  $T_\pi = 256$  MeV, shown in Fig. 14, we predict a more gradual dip-bump angular dependence, which also agrees with the experimental data. At the same time, our theoretical curves do not reproduce the data for  $T_\pi = 142$  MeV, shown in Fig. 11, even though the angular dependence is much smoother. We note, however, that the amount of experimental data for  $T_\pi = 220$  and 256 MeV is significantly less than for  $T_\pi = 142$  and especially for 180 MeV. Evaluation of the  $T_\pi = 142$  MeV data may require an additional mechanism to reproduce the behavior of the data. <sup>3</sup>

## VI. ADDITIONAL REMARKS

### A. $\Delta_{33}$ -Mass Splitting and Total Cross Sections

We have seen that one of the principal sources of CSV is the  $\Delta_{33}$ -mass splitting. The difference in the total  $\pi^\pm d$  cross sections is determined by the  $\Delta_{33}$ -mass splitting [17]. Here, we calculate this effect for the ratios  $r_{1t}$  and  $r_{2t}$  for the *total* cross sections of  $\pi^\pm{}^3H/{}^3He$  scattering, defined as

$$r_{1t} = \frac{\sigma^{tot}(\pi^+{}^3H)}{\sigma^{tot}(\pi^-{}^3He)} \text{ and } r_{2t} = \frac{\sigma^{tot}(\pi^-{}^3H)}{\sigma^{tot}(\pi^+{}^3He)}.$$

We predict a considerably larger CSV effect for the three-nucleon system than for the deuteron, as shown in Fig. 15. Moreover, the crossover of  $r_{1t}$  and  $r_{2t}$  at the peak of the  $\Delta_{33}$ , for either of the WFs used, establishes a unique signature for this effect.

The high sensitivity of CSV to the  $N^*$ -mass splitting (within multiplets) allows us to suggest the use of these ratios as a method to determine the mass-splitting in heavy  $N^*$ s and  $\Delta^*$ s. We think that this method would be preferable to the traditional  $\pi N$  partial-wave analysis for baryon spectroscopy.

### B. Accuracy of Calculations

In our theoretical approach to single and double scattering, we neglect the Fermi motion of the nucleons inside the nucleus. The amplitude of the  $\pi N$  scattering is extracted from an integral over incident pion energies that are on-shell. We also neglect the recoil of the nucleons in the Green's function  $G_\pi$  of Eq. (14) for the double-scattering amplitude. We call this approach the “fixed-centers approximation.” Then, we observe that when only certain corrections are taken into account, we obtain worse agreement with the experimental data (see Ref. [20] for details).

Since the fixed-centers approximation gives results that are close to the data, there must be cancellations of the main corrections to leading order. These cancellations for hadron-deuteron scattering have been discussed in detail in previous work. The cancellation of

---

<sup>3</sup>In the most advanced study [15], the authors considered only the case for  $T_\pi = 180$  MeV. On the other hand, the calculation of Ref. [14] does not reproduce the CSV effect for 142 MeV either.



nonadiabatic corrections within the Glauber approach for differential cross sections at high energies was shown in Ref. [29]. In the  $\pi d$  scattering-length calculations, the cancellation of off-shell and recoil corrections was discussed in Ref. [30]. The cancellation of nonadiabatic corrections for  $\pi d$  elastic scattering was found in the range of the  $\Delta_{33}$  resonance in Ref. [31]. Apparently, the analogous cancellation of corrections holds as well for the  $A = 3$  nuclei. Therefore, the use of only a few of the corrections to the fixed-centers approximation can result in worse agreement with the data than when all the corrections are ignored. Inclusion of all the corrections (including the so-called binding corrections) is a rather complicated task and is not a goal of our present study.

For example, we limit ourselves to the consideration of single- and double-scattering terms, and this approach allows us to take into account the leading terms of the amplitude of the pion-nuclear interaction at energies and scattering angles where we can qualitatively reproduce the shape of the distribution of the differential cross sections. Triple-scattering contributions to the differential cross sections can smooth the angular shape, but they are more difficult to calculate and cannot be simplified by the transformation of the integrals  $J_1$  and  $J_2$  discussed in Appendix B.

### C. Pion Absorption

At small scattering angles,  $\theta \sim 30^\circ - 60^\circ$ , there is reasonable agreement between our theoretical approach and the experimental data for  $T_\pi = 180$  MeV and above, but for  $T_\pi = 142$  MeV the experimental cross sections are smaller than the results of our model calculations for both WFs used (Figs. 3 – 6). But because for modest scattering angles the range of momentum transfer is small ( $Q \leq 150$  MeV/c), our use of the simple WFs (7) and (8) is reasonable. We therefore infer that the suppression of the cross section for  $T_\pi = 142$  MeV results from absorption, which is absent in our model approach for the amplitude of the  $\pi A$  interaction. Usually, the absorption on a nucleus is due to the reaction  $\pi(NN) \rightarrow NN$ , where  $(NN)$  is a pair of correlated nucleons. But the total cross section of the  $\pi d \rightarrow NN$  reaction has its maximum at  $T_\pi = 140$  MeV, and the absorption cross section is somewhat suppressed at  $T_\pi = 180$  MeV [32]. However,  $T_\pi = 180$  MeV corresponds to the maximum of the total  $\pi^\pm d$  cross section, as shown in Fig. 16. The pion absorption cross section for  ${}^3\text{He}$ , measured at PSI [33], also peaks at  $T_\pi = 140 - 150$  MeV, as shown in Fig. 16 as well. Therefore, if absorption were responsible for the suppression of the scattering cross sections at small scattering angles for  $T_\pi = 142$  MeV, then this effect would be considerably smaller for  $T_\pi = 180$  MeV, where our fit to the data is much better.

### D. CSV in $\pi^\pm {}^4\text{He}$ Elastic Scattering

Data for the elastic  $\pi^\pm {}^4\text{He}$  differential cross sections have been obtained at LAMPF for  $T_\pi$  below, at, and above the  $\Delta_{33}$  resonance [34]. The spin-flip amplitudes for elastic  $\pi^\pm {}^4\text{He}$  in the single-scattering approximation do not contribute to the  $\Delta_{33}$  resonance. Preliminary analysis of the charge asymmetry for  $T_\pi = 180$  MeV shows a statistically significant effect in  $A_\pi$ , of the order of 10% at scattering angles  $\theta \sim 70^\circ - 90^\circ$  [35]. The size of  $A_\pi$  for  $T_\pi \leq 180$  MeV and the possible influence of absorption there are still unknown.

Because of the larger role played by pion absorption on heavier nuclei, CSV is expected to be suppressed relative to the three- and four-body nuclei. If present, CSV in heavier nuclei probably depends more on their geometrical properties than on the  $\Delta_{33}$ -mass splitting.

## VII. SUMMARY

We have performed theoretical calculations for the simple ratios  $r_1$  and  $r_2$  and the superratio  $R$  for elastic  $\pi^{\pm 3}H/{}^3He$  scattering, for  $T_\pi = 142, 180, 220,$  and  $256$  MeV and over a broad angular range. We have found reasonable agreement between the results of our calculations and the experimental data, shown in Fig. 1, over most of the range of the data.

Our calculations were done in an approach utilizing the sum of the single- and double-scattering  $\pi N$  contributions, as indicated in Fig. 2. We took into account three sources of CSV – the  $\Delta_{33}$ -mass splitting and the external and internal Coulomb interactions. We used  $S$ -shell WFs for  ${}^3H$  and  ${}^3He$ . This approach enabled us to use simple analytical expressions for the double-scattering contribution to pion-nuclear scattering, taking into account all spin and isospin amplitudes. We used two different radial WFs for the  $A = 3$  nuclei:

i) A simple Gaussian distribution (Eq. (7)) with the slope describing the charge densities of  ${}^3H$  and  ${}^3He$  obtained from electron scattering [21,36–38]. We used the WF of Ref. [14].

ii) A sum of two Gaussian WFs (Eq. (8)), as used in Ref. [22] for the description of the differential cross sections of the reaction  ${}^4He(p, d){}^3He$ . This WF reproduces the minimum of the  ${}^3He$  charge form factor at  $Q = 670$  MeV/c, but shows an enhancement at smaller momentum transfer.

The calculated cross sections, shown in Figs. 3 – 6, agree qualitatively with the experimental data. For  $T_\pi = 180$  MeV, the theoretical curves have minima at  $\theta \sim 140^\circ - 150^\circ$  and reproduce the gradual growth of the cross sections as  $\theta$  approaches  $180^\circ$ , indicating the importance of the inclusion of double scattering for the differential cross sections. Of course, the absolute cross sections are very sensitive to the WF, and are not reproduced well by the simple  $S$ -shell approach used here.

The main goal of our study is the calculation of the CSV effects for  $\pi^{\pm 3}H/{}^3He$  differential cross sections in terms of the observables  $r_1$ ,  $r_2$ , and  $R$ . No free parameters are used in our approach in taking into account the  $\Delta_{33}$ -mass splitting and the external Coulomb interaction. Figures. 8 – 10 show that these factors alone account qualitatively for major features of the data. These figures also show that there is little sensitivity to the choice of the wave function.

Figures 12 – 14 show that when the internal Coulomb effect is included as well, there is reasonable agreement between our theoretical calculations and the experimental data. The best agreement is found for  $T_\pi = 180$  MeV (at the peak of the  $\Delta_{33}$  resonance). Both the  $\Delta_{33}$ -mass splitting and the internal Coulomb interaction are important for the reproduction of the shape of the angular distribution, both near the non-spin-flip dip at  $\theta \sim 80^\circ$  and at large scattering angles. Although the influence of the internal Coulomb interaction on CSV has been shown before [15], our investigation shows that including the  $\Delta_{33}$ -mass splitting results in a still better description of the effect of CSV, as it should: the  $\Delta_{33}$ -mass splitting

exists, so its effects should not be ignored. We also predict the simple mirror ratios for the total cross sections, as shown in Fig. 15.

Finally, however, as seen from Figs. 7 and 11, our calculations do not reproduce the data for  $T_\pi = 142$  MeV. Although we tried to take into account a number of different approaches beyond the framework of our model (more accurate amplitudes for single and double scattering and Fermi motion, *etc.*), we were not able to improve the agreement for  $T_\pi = 142$  MeV. Therefore, the question of the nature of the effect of CSV for  $T_\pi = 142$  MeV remains open. Perhaps there is an additional mechanism at  $T_\pi = 142$  MeV which does not manifest itself at higher energies; Fig. 16 shows that quite possibly, pion absorption plays a major role.

### ACKNOWLEDGMENTS

The authors acknowledge very useful communications with B. V. Geshkenbein, S. S. Kamalov, and C. L. Morris. This work was supported in part by the U. S. Department of Energy under Grants DE-FG02-95ER40901 and DE-FG02-99ER41110 and by the Russian Grants for Basic Research N 98-02-17618 and N 00-15-96562. A. K. acknowledges the hospitality extended by the Center for Nuclear Studies of The George Washington University. I. S. acknowledges partial support from Jefferson Lab, by the Southeastern Universities Research Association under DOE contract DE-AC05-84ER40150.

### APPENDIX A: THE CHARGE FORM FACTOR $F(\vec{\Delta})$

Let us introduce relative coordinates of the nucleons  $\vec{\rho}_i = \vec{r}_j - \vec{r}_k$  and  $\vec{R}_i = \frac{1}{2}(\vec{r}_j + \vec{r}_k) - \vec{r}_i$  instead of  $\vec{r}_i$ . In terms of these new variables, the function  $\psi$  of Eq. (5) yields

$$\psi(\vec{r}_1, \vec{r}_2, \vec{r}_3) \equiv \psi\left(\sum_{m=1}^3 (\vec{r}_i - \vec{R}_0)^2\right) = \psi\left(\frac{\vec{\rho}_i^2}{2} + \frac{2}{3}\vec{R}_i^2\right) = \psi(\vec{\rho}, \vec{R}). \quad (\text{A1})$$

This function  $\psi$  does not depend on the selection of a basis  $i(jk)$ . The Fourier transformation of the function  $\psi$  is defined by

$$\varphi(\vec{q}, \vec{Q}) = \int d^3\vec{\rho} d^3\vec{R} \psi(\vec{\rho}, \vec{R}) \exp(-i\vec{q} \cdot \vec{\rho} - i\vec{Q} \cdot \vec{R}), \quad (\text{A2})$$

where  $\vec{q} = \vec{q}_i = (\vec{p}_j - \vec{p}_k)/2$  and  $\vec{Q} = \vec{Q}_i = (\vec{p}_j + \vec{p}_k - 2\vec{p}_i)/3$  are relative momenta and  $(\vec{p}_i, \vec{p}_j, \vec{p}_k)$  are the momenta of the nucleons of the nucleus. For the WF (8),  $\varphi(\vec{q}, \vec{Q})$  has the form

$$\varphi(\vec{q}, \vec{Q}) = N \left(\frac{\pi}{\sqrt{12}}\right) \sum_m \frac{D_m}{\alpha_m^3} \exp\left(-\frac{q^2}{\alpha_m} - \frac{3Q^2}{4\alpha_m}\right), \quad (\text{A3})$$

where

$$N^{-2} = \frac{9}{2}(\pi\sqrt{12})^3 \sum_{m,n} \frac{D_m D_n}{(\alpha_m + \alpha_n)^2}.$$

The charge form factor for elastic scattering is defined by

$$F(\vec{\Delta}) = \frac{9}{2} \int \frac{d\vec{q}}{(2\pi)^3} \frac{d\vec{Q}}{(2\pi)^3} \varphi(\vec{q}, \vec{Q} - \frac{2}{3}\vec{\Delta}) \varphi(\vec{q}, \vec{Q}), \quad F(0) = 1. \quad (\text{A4})$$

An analytical expression for the form factor (A4) corresponding to the WF (8) is

$$F(\vec{\Delta}) = N_0^{-1} \sum_{m,n} \frac{D_m D_n}{(\alpha_m + \alpha_n)^3} \exp\left[-\frac{\Delta^2}{3(\alpha_m + \alpha_n)}\right], \quad (\text{A5})$$

where

$$N_0 = \sum_{m,n} \frac{D_m D_n}{(\alpha_m + \alpha_n)^3}.$$

## APPENDIX B: THE TENSOR $I_{ij}$ AND THE FUNCTIONS $J_1$ AND $J_2$

The expression for the tensor  $I_{ij}$  in terms of the wave function  $\varphi(\vec{q}, \vec{Q})$  (A2) is

$$I_{ij} = 4\pi \int \frac{d^3\vec{q}}{(2\pi)^3} \frac{d^3\vec{Q}}{(2\pi)^3} \frac{d^3\vec{Q}'}{(2\pi)^3} \varphi(\vec{q}', \vec{Q}') \varphi(\vec{q}, \vec{Q}) \frac{\hat{s}_i \hat{s}_j}{k_1^2 - s^2 - i0}. \quad (\text{B1})$$

This integral is suitable for calculations in coordinate space. To do this, we follow a transformation first used in Ref. [31]:

$$\frac{\hat{s}_i \hat{s}_j}{k_1^2 - s^2 - i0} = \frac{1}{4\pi} \int \exp(i\vec{s} \cdot \vec{r}) H_{ij}(\vec{r}) d\vec{r}, \quad (\text{B2})$$

where

$$H_{ij}(\vec{r}) = h_1(r) \hat{r}_i \hat{r}_j + h_2(r) \delta_{ij}$$

and

$$h_1(r) = \frac{e^{ikr}}{r} + \frac{3ie^{ikr}}{kr^2} - \frac{3e^{ikr}}{k^2 r^3} + \frac{3}{k^2 r^3},$$

$$h_2(r) = \frac{e^{ikr}}{k^2 r^3} - \frac{1}{k^2 r^3} - \frac{ie^{ikr}}{kr^2}.$$

Then, using Eq. (B2) and the coordinate expression for the wave function (A1), we get the expression for the tensor  $I_{ij}$ :

$$I_{ij} = \frac{2}{9} \int d^3\vec{\rho} d^3\vec{r} \psi^2(\vec{\rho}, \vec{R}) H_{ij}(\vec{r}) \exp[i(\vec{k}_1 - \frac{\vec{\Delta}}{3}) \cdot \vec{r} + i\frac{\vec{\Delta} \cdot \vec{\rho}}{3}], \quad (\text{B3})$$

where  $\vec{R} = \vec{r} + \frac{1}{2}\vec{\rho}$ . If the WF  $\psi(\vec{\rho}, \vec{R})$  is expressed as a sum of several Gaussians, the integral (B3) can be represented in the form of expression (20). Then the integrals  $J_1$  and  $J_2$  are transformed into one-dimensional integrals. For the WF (8), they have the form

$$J_{1,2} = \frac{2}{9} N^2 \sum_{m,n} D_m D_n \left(\frac{3\pi}{a_{mn}}\right)^{1/2} \exp\left(-\frac{\Delta^2}{12a_{mn}}\right) F_{1,2}(a_{mn}, \theta),$$

$$\begin{aligned}
\text{where } F_1(a, \theta) &= \pi \int_0^\infty r^2 \exp\left(\frac{ar^2}{4}\right) (3E_2 - E_0) h_1(r) dr, \\
F_2(a, \theta) &= \pi \int_0^\infty r^2 \exp\left(\frac{ar^2}{4}\right) [(E_0 - E_2) h_1(r) + 2E_0 h_2(r)] dr, \\
E_n &= \int_{-1}^1 \exp(i\xi r z) z^n dz,
\end{aligned} \tag{B4}$$

$\xi = k \cos \frac{\theta}{2}$ ,  $\Delta = 2k \sin \frac{\Delta}{2}$ , and  $N$  is given by Eq. (A3). In the case of WF (7), the expressions for the integrals  $J_{1,2}$  are computed easily from Eq. (B4).

## REFERENCES

- [1] G. A. Miller, B. M. K. Nefkens, and I. Slaus, Phys. Rep. **194**, 1 (1990).
- [2] S. Weinberg, in: *Chiral Dynamics: Theory and Experiment*, eds. A. M. Bernstein and B. R. Holstein, Springer (1994) p. 3.
- [3] U.-G. Meissner, in: *Proc. of 9th International Symposium on Meson-Nucleon Physics and the Structure of the Nucleon, Washington, DC, USA, July 26–31, 2001*, Eds. H. Haberzettl and W. J. Briscoe,  $\pi N$  Newslett. **16**, 1 (2001), to be published.
- [4] A. Gashi, E. Matsinos, G. C. Oades, G. Rasche, and W. S. Woolcock, Eprint nucl-th/0009081, submitted to Nucl. Phys. **A**.
- [5] T. G. Masterson, J. J. Kraushaar, R. J. Peterson, R. S. Raymond, R. A. Ristinen, R. L. Boudrie, E. F. Gibson, and A. W. Thomas, Phys. Rev. C **26**, 2091 (1982).
- [6] V. V. Baru, A. E. Kudryavtsev, V. E. Tarasov, W. J. Briscoe, K. S. Dhuga, and I. I. Strakovsky, Phys. Rev. C **62**, 044003 (2000).
- [7] B. M. K. Nefkens, W. J. Briscoe, A. D. Eichon, D. H. Fitzgerald, A. Mokhtari, and J. A. Wightman, Phys. Rev. C **41**, 2770 (1990).
- [8] C. Pillai, D. B. Barlow, B. L. Berman, W. J. Briscoe, A. Mokhtari, B. M. K. Nefkens, and M. E. Sadler, Phys. Rev. C **43**, 1838 (1991).
- [9] K. S. Dhuga, B. L. Berman, W. J. Briscoe, R. W. Caress, S. K. Matthews, D. B. Barlow, B. M. K. Nefkens, C. Pillai, J. W. Price, S. J. Greene, I. Slaus, and I. Supek, Phys. Rev. C **54**, 2823 (1996).
- [10] W. J. Briscoe *et al.*, in preparation for submission to Phys. Rev. C.
- [11] B. L. Berman G. C. Anderson, W. J. Briscoe, A. Mokhtari, A. M. Petrov, M. E. Sadler, D. B. Barlow, B. M. K. Nefkens, and C. Pillai, Phys. Rev. C **51**, 1882 (1995).
- [12] S. K. Matthews, W. J. Briscoe, C. Bennhold, B. L. Berman, R. W. Caress, K. S. Dhuga, S. N. Dragic, S. S. Kamalov, N. J. Nicholas, M. F. Taragin, L. Tiator, S. J. Greene, D. B. Barlow, B. M. K. Nefkens, C. Pillai, J. W. Price, L. D. Isenhower, M. E. Sadler, I. Slaus, and I. Supek, Phys. Rev. C **51**, 2534 (1995).
- [13] K. T. Kim, Y. E. Kim, and R. H. Landau, Phys. Rev. C **36**, 2155 (1987).
- [14] S. S. Kamalov, L. Tiator, and C. Bennhold, Phys. Rev. C **47**, 941 (1993).
- [15] W. R. Gibbs and B. F. Gibson, Phys. Rev. C **43**, 1012 (1991).
- [16] E. Pedroni, K. Gabathuler, J. J. Domingo, W. Hirt, P. Schwaller, J. Arvieux, C. H. Q. Ingram, P. Gretillat, J. Piffaretti, N. W. Tanner, and C. Wilkin, Nucl. Phys. **A300**, 321 (1978).
- [17] T. Ericson and W. Weise, *Pions and Nuclei*, Clarendon Press, Oxford, 1988.
- [18] G. R. Smith *et al.*, Phys. Rev. C **38**, 240 (1988).
- [19] S. K. Matthews, “Elastic scattering of pions from tritium and  $^3\text{He}$  in the backward hemisphere in the region of the  $\Delta_{33}(1232)$  resonance,” Ph. D. thesis, The George Washington University, 1993 (unpublished).
- [20] W. J. Briscoe, A. E. Kudryavtsev, I. I. Strakovsky, and V. E. Tarasov, Phys. At. Nucl. (former Sov. J. Nucl. Phys.) **64**, 1430 (2001).
- [21] F.-P. Juster, S. Auffret, J.-M. Cavedon, J.-C. Clemens, B. Frois, D. Goutte, M. Huet, P. Leconte, J. Martino, Y. Mizuno, X.-H. Phan, S. Platchkov, and S. Williamson, Phys. Rev. Lett. **55**, 2261 (1985).
- [22] A. Foursat, E. Lyovshin, and K. Sailer, Nucl. Phys. **A392**, 399 (1983).
- [23] R. H. Landau, Computer Phys. Comm. **28**, 109 (1982).

- [24] S. L. Collier and W. R. Gibbs, *Phys. Rev. C* **59**, 1290 (1999).
- [25] R. A. Arndt, R. L. Workman, I. I. Strakovsky, and M. M. Pavan, Eprint nucl-th/9807087, submitted to *Phys. Rev. C*.
- [26] S. R. Amendolia *et al.*, *Nucl. Phys.* **B277**, 168 (1986).
- [27] S. Weinberg and S. B. Treiman, *Phys. Rev.* **116**, 465 (1959).
- [28] D. E. Groom *et al.*, *Review of Particle Physics*, *Eur. Phys. J. C* **15**, 1 (2000).
- [29] V. M. Kolybasov and L. A. Kondratyuk, *Phys. Lett.* **B39**, 439 (1972).
- [30] G. Fäldt, *Phys. Scripta*, **16**, 81 (1977); V. M. Kolybasov and V. G. Ksenzov, *JETP* **71**, 13 (1976); V. G. Ksenzov, *Phys. Atom. Nucl. (former Sov. J. Nucl. Phys.)* **28**, 644 (1978); O. D. Dalkarov, V. M. Kolybasov, and V. G. Ksenzov, *Nucl. Phys.* **A397**, 498 (1983); V. V. Baru and A. E. Kudryavtsev, *Phys. Atom. Nucl. (former Sov. J. Nucl. Phys.)* **60**, 1475 (1997).
- [31] V. M. Kolybasov and A. E. Kudryavtsev, *Phys. Atom. Nucl. (former Sov. J. Nucl. Phys.)* **17**, 42 (1973).
- [32] C. H. Oh, R. A. Arndt, I. I. Strakovsky, and R. L. Workman, *Phys. Rev. C* **56**, 635 (1997).
- [33] A. Lehmann *et al.*, *Phys. Rev. C* **55**, 2931 (1997).
- [34] B. Brinkmüller *et al.*, *Phys. Rev. C* **44**, 2031 (1991).
- [35] C. L. Morris, private communication, 2000.
- [36] J. S. McCarthy, I. Sick, and R. R. Whitney, *Phys. Rev. C* **15**, 1396 (1977).
- [37] D. Beck *et al.*, *Phys. Rev. Lett.* **59**, 1537 (1987).
- [38] A. Amroun, V. Breton, J.-M. Cavedon, B. Frois, D. Goutte, J. Martino, X.-H. Phan, S. K. Platchkov, I. Sick, and S. Williamson, *Phys. Rev. Lett.* **69**, 253 (1992).

TABLES

TABLE I. Best-fit results for the ratios  $r_1$  and  $r_2$  from variation of the  ${}^3H$  and  ${}^3He$  WFs. The slope  $b$  has been varied for the WF (7) [14]. Cases (i) – (iii) of variations of the WF (8) [22] have been discussed in the text. Differences in the mean-square charge radii  $\delta r = r({}^3He) - r({}^3H)$  and  $\chi^2/d.f.$  are listed in columns 5 and 6. The last column shows  $\chi^2/d.f.$  when the internal Coulomb interaction is not taken into account.

$T_\pi$ (MeV)	WF	Varied Parameter		$\delta r$ (fm)	$\chi^2/d.f.$	$\chi^2/d.f. (\delta r \equiv 0)$
142	[14]	b		0.015	3.90	4.87
	[22]	$\alpha_1$	(i)	0.017	4.15	5.06
		$\alpha_2$	(ii)	0.010	4.44	
		$\alpha_1$ and $\alpha_2$	(iii)	0.014	4.26	
180	[14]	b		0.012	1.68	2.88
	[22]	$\alpha_1$	(i)	0.017	1.60	3.05
		$\alpha_2$	(ii)	0.014	1.65	
		$\alpha_1$ and $\alpha_2$	(iii)	0.016	1.61	
220	[14]	b		0.019	8.46	10.5
	[22]	$\alpha_1$	(i)	0.016	5.37	6.74
		$\alpha_2$	(ii)	0.011	5.37	
		$\alpha_1$ and $\alpha_2$	(iii)	0.014	5.36	
256	[14]	b		-0.010	2.26	2.43
	[22]	$\alpha_1$	(i)	-0.006	2.29	2.37
		$\alpha_2$	(ii)	0	2.37	
		$\alpha_1$ and $\alpha_2$	(iii)	-0.003	2.35	



## Figure captions

Figure 1. The ratios  $r_1$ ,  $r_2$ , and the superratio  $R$  for  $\pi^{\pm 3}H/{}^3He$  elastic scattering for various incident pion kinetic energies: (a)  $T_\pi = 142$  MeV, (b) 180 MeV, (c) 220 MeV, and (d) 256 MeV. Experimental data are from [7] (diamonds), [8] (circles), [9] (triangles), and [10] (squares).

Figure 2. (a) Single- and (b) double-scattering diagrams used in the present calculations for  $\pi^{\pm 3}H/{}^3He$  elastic scattering.

Figure 3. Differential cross sections for  $\pi^{\pm 3}H/{}^3He$  elastic scattering for  $T_\pi = 142$  MeV. Plotted are results for (a,b) WFs (7) and (c,d) WF (8). Experimental data are from [7] (diamonds), [8] (circles), [9] (triangles), and [10] (squares), with  $\pi^+{}^3He/{}^3H$  (filled) and  $\pi^-{}^3He/{}^3H$  (open). The cross sections (a,c) are for  $\pi^+{}^3He$  and  $\pi^-{}^3H$  and (b,d) for  $\pi^+{}^3H$  and  $\pi^-{}^3He$ . The solid curves give the total contribution. Results for single and double scattering alone are shown by the dashed and dotted curves, respectively.

Figure 4. Differential cross sections for  $\pi^{\pm 3}H/{}^3He$  elastic scattering for  $T_\pi = 180$  MeV. The notation is the same as for Fig. 3.

Figure 5. Differential cross sections for  $\pi^{\pm 3}H/{}^3He$  elastic scattering for  $T_\pi = 220$  MeV. The notation is the same as for Fig. 3.

Figure 6. Differential cross sections for  $\pi^{\pm 3}H/{}^3He$  elastic scattering for  $T_\pi = 256$  MeV. The notation is the same as for Fig. 3.

Figure 7. The ratios  $r_1$  and  $r_2$  and the superratio  $R$  for  $T_\pi = 142$  MeV. The notation for the experimental data is the same as for Fig. 1. Only the  $\Delta_{33}$ -mass splitting and external Coulomb contributions are taken into account. The full calculations take into account both single and double scattering, and are shown by the dashed curves. The results for single scattering alone are shown by the dotted curves. Plotted are the results for (a) WF (7) and (b) WF (8).

Figure 8. The ratios  $r_1$  and  $r_2$  and the superratio  $R$  for  $T_\pi = 180$  MeV. The notation is the same as for Fig. 7.

Figure 9. The ratios  $r_1$  and  $r_2$  and the superratio  $R$  for  $T_\pi = 220$  MeV. The notation is the same as for Fig. 7.

Figure 10. The ratios  $r_1$  and  $r_2$  and the superratio  $R$  for  $T_\pi = 256$  MeV. The notation is the same as for Fig. 7.

Figure 11. The ratios  $r_1$  and  $r_2$  and the superratio  $R$  for  $T_\pi = 142$  MeV. The notation for the experimental data is the same as for Fig. 1. The  $\Delta_{33}$ -mass splitting with external (and internal) Coulomb contributions are shown by the dashed (solid) curves. Plotted are the results for (a) WF (7) and (b) WF (8). Version (iii) of the variation of the WFs is shown, as described in Sec. IV.

Figure 12. The ratios  $r_1$  and  $r_2$  and the superratio  $R$  for  $T_\pi = 180$  MeV. The notation is the same as for Fig. 11.

Figure 13. The ratios  $r_1$  and  $r_2$  and the superratio  $R$  for  $T_\pi = 220$  MeV. The notation is the same as for Fig. 11.

Figure 14. The ratios  $r_1$  and  $r_2$  and the superratio  $R$  for  $T_\pi = 256$  MeV. The notation is the same as for Fig. 11.

Figure 15. Predictions for the ratios  $r_{1t}$  (solid), and  $r_{2t}$  (dashed) for the total  $\pi^{\pm 3}H/{}^3He$  cross sections. Calculations were done for single and double scattering with the  $\Delta_{33}$ -mass splitting. The Coulomb interactions are not taken into account. Plotted are the results for (a) WF (7) and (b) WF (8).

Figure 16. Total  $\pi^+$  cross sections. Plotted are cross sections for  $\pi^+d$  (solid) and  $\pi^+d \rightarrow pp$  (multiplied by a factor of 20) (dashed) from a recent combined fit of the  $pp$  and  $\pi d$  elastic scattering with the  $\pi^+d \rightarrow pp$  data [32]. The  $\pi^3He$  absorption data (multiplied by a factor of 10) are from [33] (filled circles); it can be seen that they peak near  $T_\pi = 140$  MeV.

## FIGURES

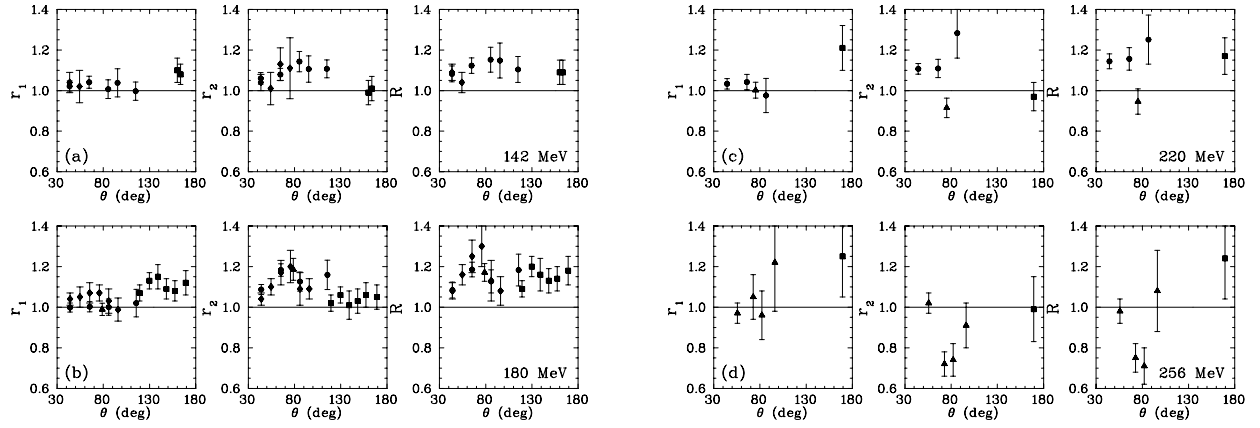


FIG. 1. The ratios  $r_1$ ,  $r_2$ , and the superratio  $R$  for  $\pi^{\pm 3}H/{}^3He$  elastic scattering for various incident pion kinetic energies: (a)  $T_{\pi} = 142$  MeV, (b) 180 MeV, (c) 220 MeV, and (d) 256 MeV. Experimental data are from [7] (diamonds), [8] (circles), [9] (triangles), and [10] (squares).

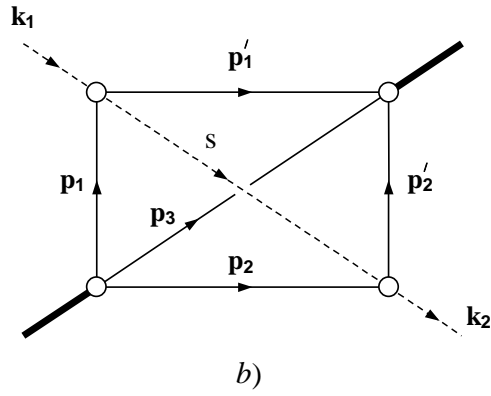
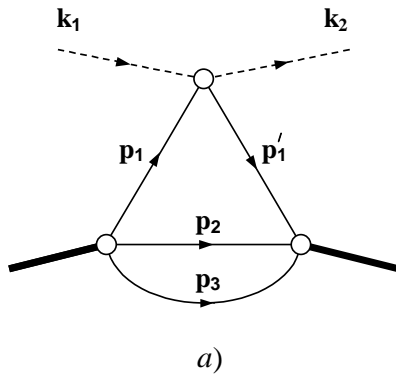


FIG. 2. (a) Single- and (b) double-scattering diagrams used in the present calculations for  $\pi^{\pm 3}H/{}^3He$  elastic scattering.

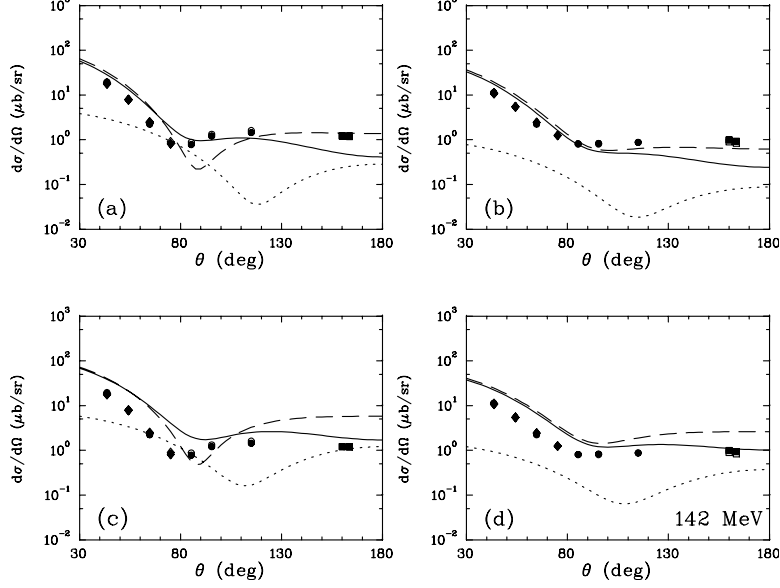


FIG. 3. Differential cross sections for  $\pi^{\pm 3}H/{}^3He$  elastic scattering for  $T_{\pi} = 142$  MeV. Plotted are results for (a,b) WFs (7) and (c,d) WF (8). Experimental data are from [7] (diamonds), [8] (circles), [9] (triangles), and [10] (squares), with  $\pi^{+3}He/{}^3H$  (filled) and  $\pi^{-3}He/{}^3H$  (open). The cross sections (a,c) are for  $\pi^{+3}He$  and  $\pi^{-3}H$  and (b,d) for  $\pi^{+3}H$  and  $\pi^{-3}He$ . The solid curves give the total contribution. Results for single and double scattering alone are shown by the dashed and dotted curves, respectively.

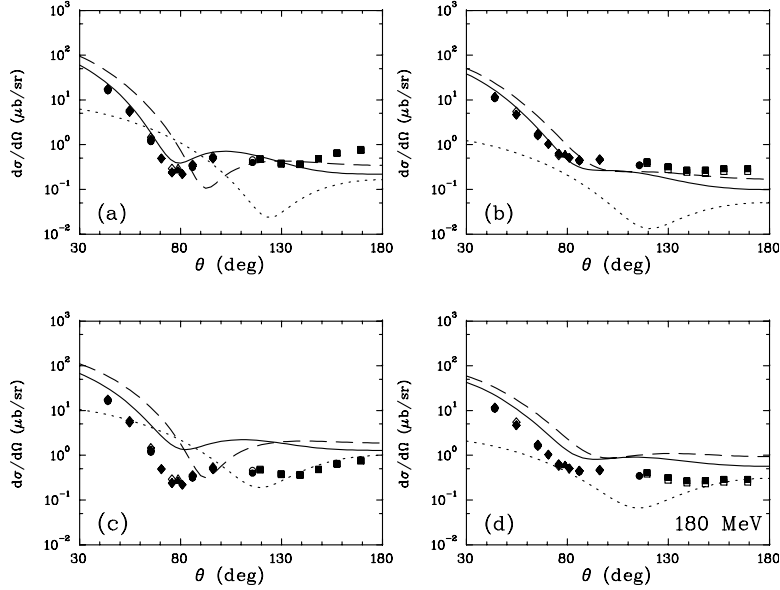


FIG. 4. Differential cross sections for  $\pi^{\pm 3}H/{}^3He$  elastic scattering for  $T_{\pi} = 180$  MeV. The notation is the same as for Fig. 3.

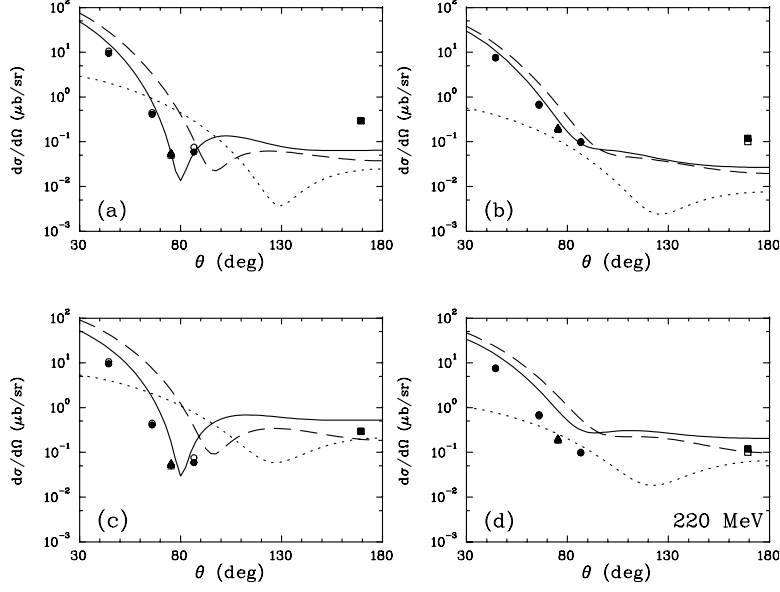


FIG. 5. Differential cross sections for  $\pi^{\pm 3}H/{}^3He$  elastic scattering for  $T_{\pi} = 220$  MeV. The notation is the same as for Fig. 3.

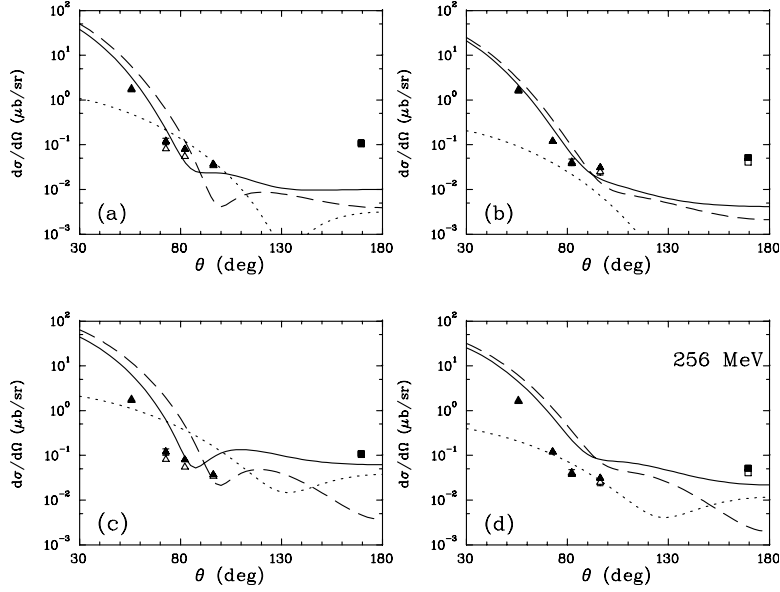


FIG. 6. Differential cross sections for  $\pi^{\pm 3}H/{}^3He$  elastic scattering for  $T_{\pi} = 256$  MeV. The notation is the same as for Fig. 3.

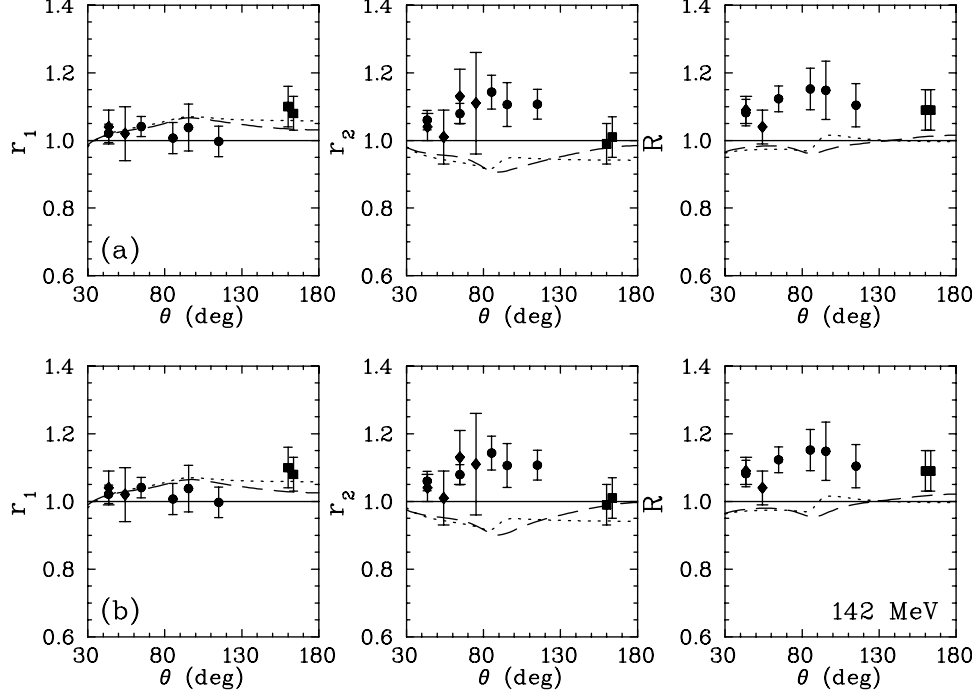


FIG. 7. The ratios  $r_1$  and  $r_2$  and the superratio  $R$  for  $T_\pi = 142$  MeV. The notation for the experimental data is the same as for Fig. 1. Only the  $\Delta_{33}$ -mass splitting and external Coulomb contributions are taken into account. The full calculations take into account both single and double scattering, and are shown by the dashed curves. The results for single scattering alone are shown by the dotted curves. Plotted are the results for (a) WF (7) and (b) WF (8).

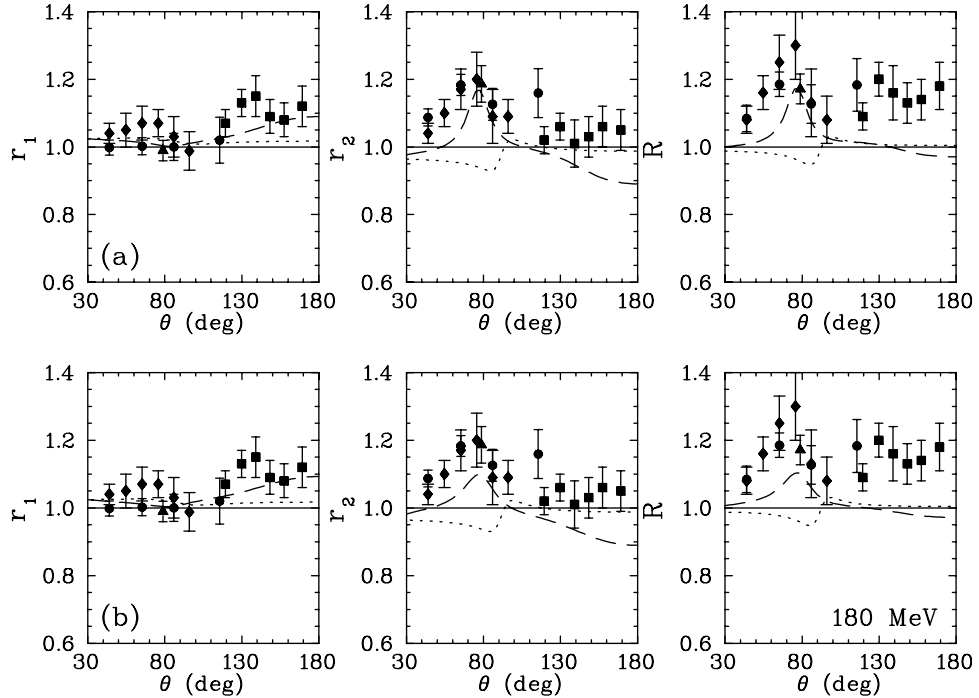


FIG. 8. The ratios  $r_1$  and  $r_2$  and the superratio  $R$  for  $T_\pi = 180$  MeV. The notation is the same as for Fig. 7.

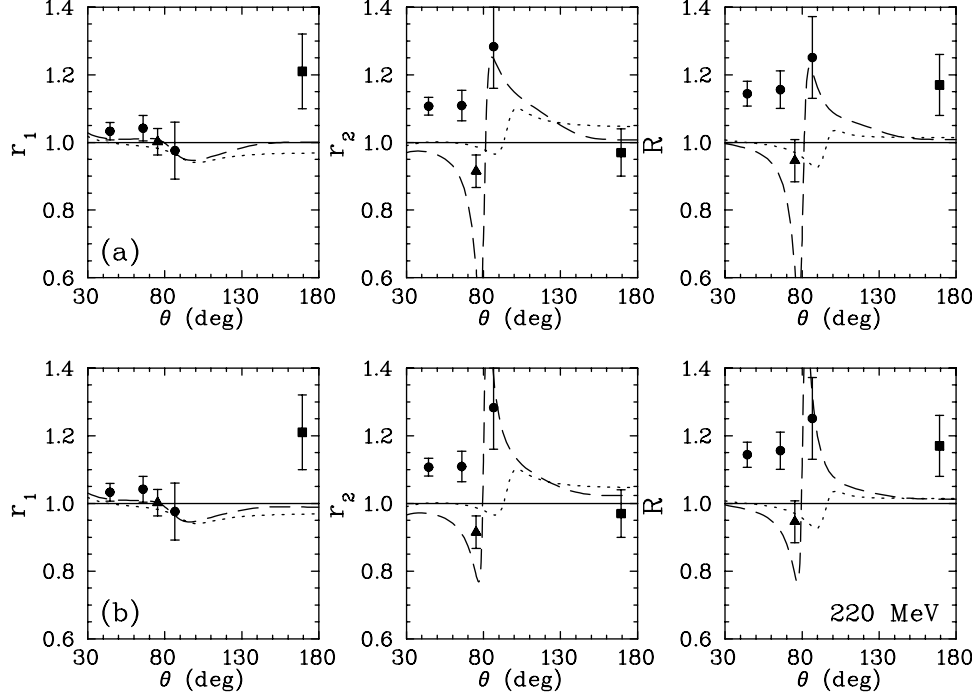


FIG. 9. The ratios  $r_1$  and  $r_2$  and the superratio  $R$  for  $T_\pi = 220$  MeV. The notation is the same as for Fig. 7.

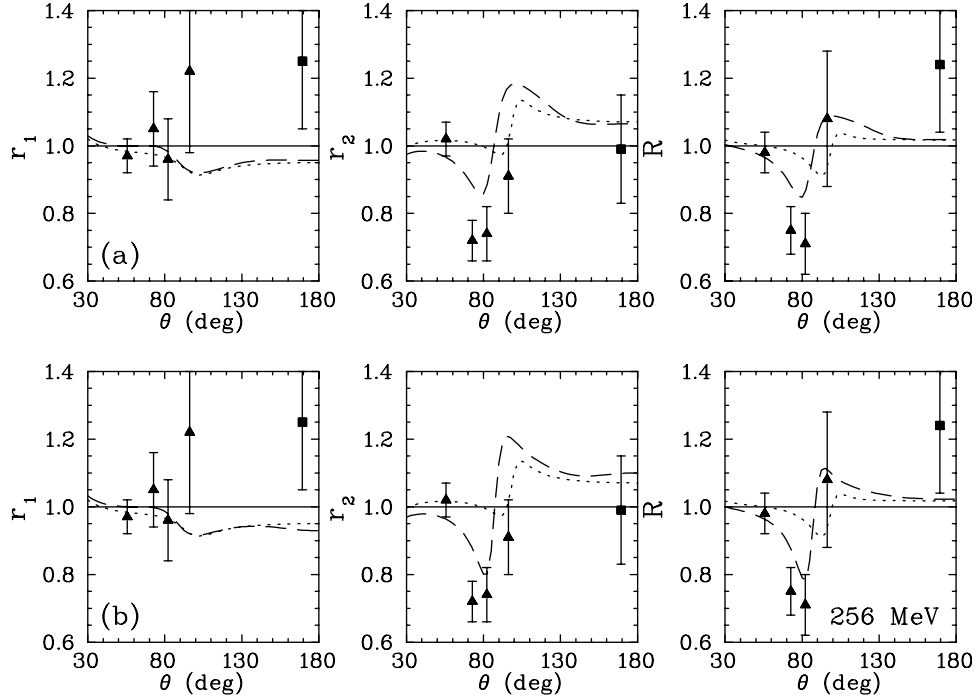


FIG. 10. The ratios  $r_1$  and  $r_2$  and the superratio  $R$  for  $T_\pi = 256$  MeV. The notation is the same as for Fig. 7.



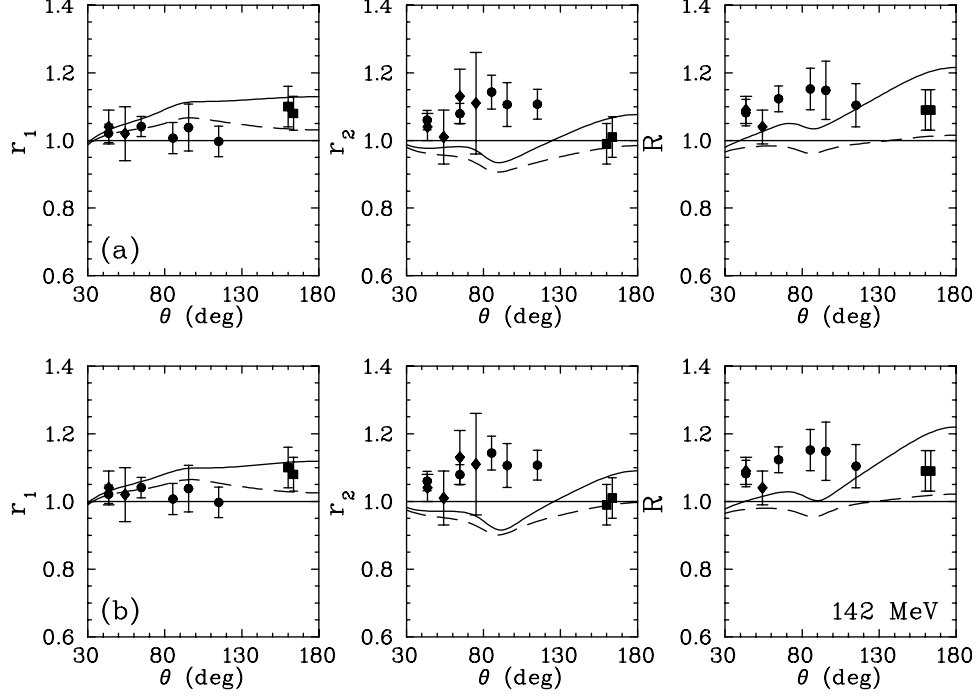


FIG. 11. The ratios  $r_1$  and  $r_2$  and the superratio  $R$  for  $T_\pi = 142$  MeV. The notation for the experimental data is the same as for Fig. 1. The  $\Delta_{33}$ -mass splitting with external (and internal) Coulomb contributions are shown by the dashed (solid) curves. Plotted are the results for (a) WF (7) and (b) WF (8). Version (iii) of the variation of the WFs is shown, as described in Sec. IV.

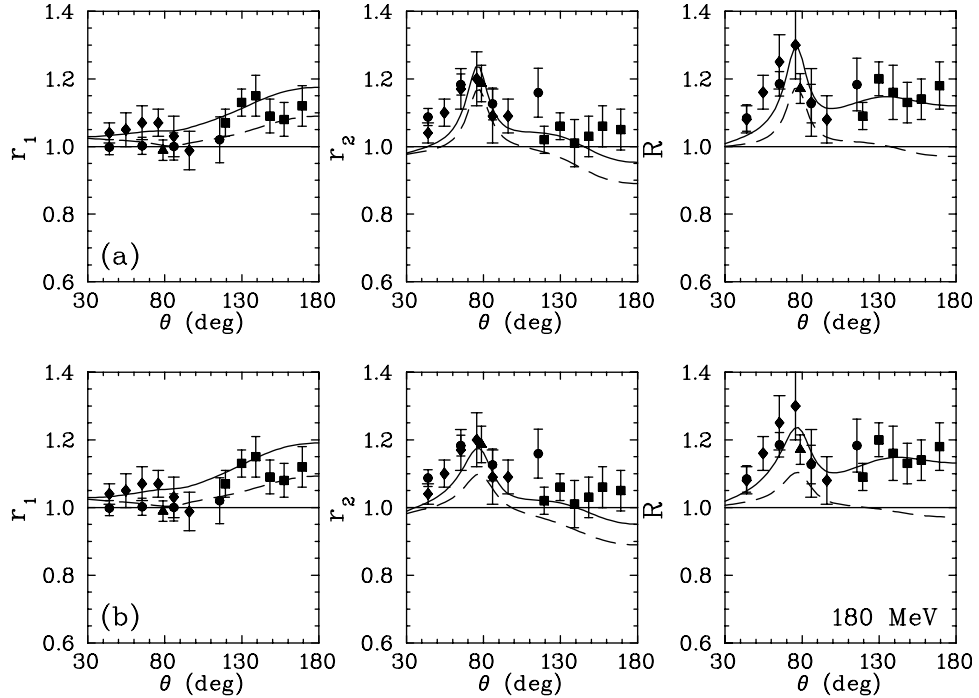


FIG. 12. The ratios  $r_1$  and  $r_2$  and the superratio  $R$  for  $T_\pi = 180$  MeV. The notation is the same as for Fig. 11.

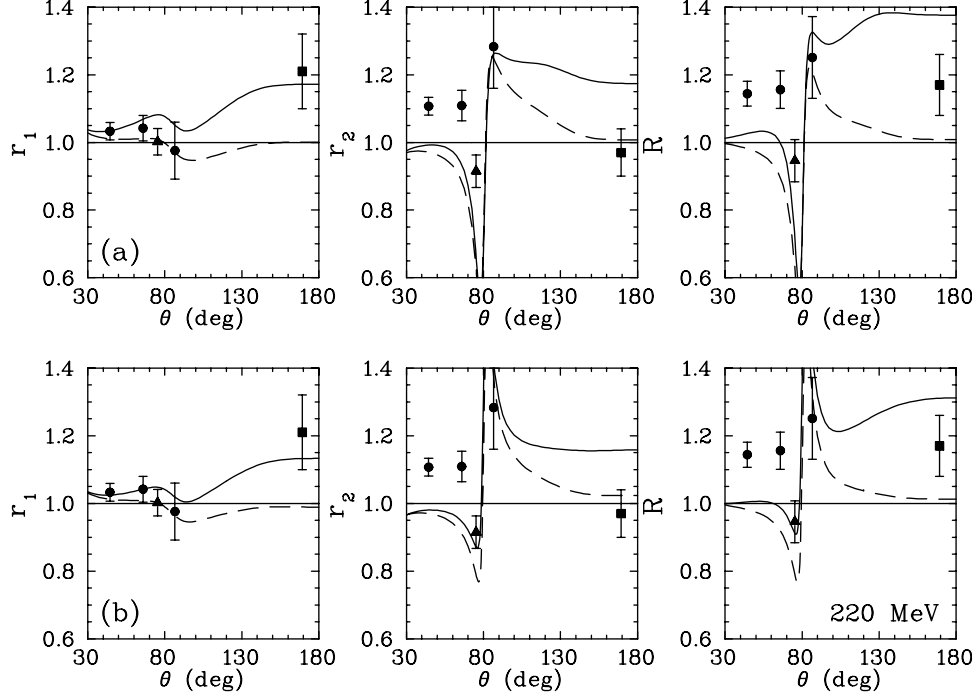


FIG. 13. The ratios  $r_1$  and  $r_2$  and the superratio  $R$  for  $T_\pi = 220$  MeV. The notation is the same as for Fig. 11.

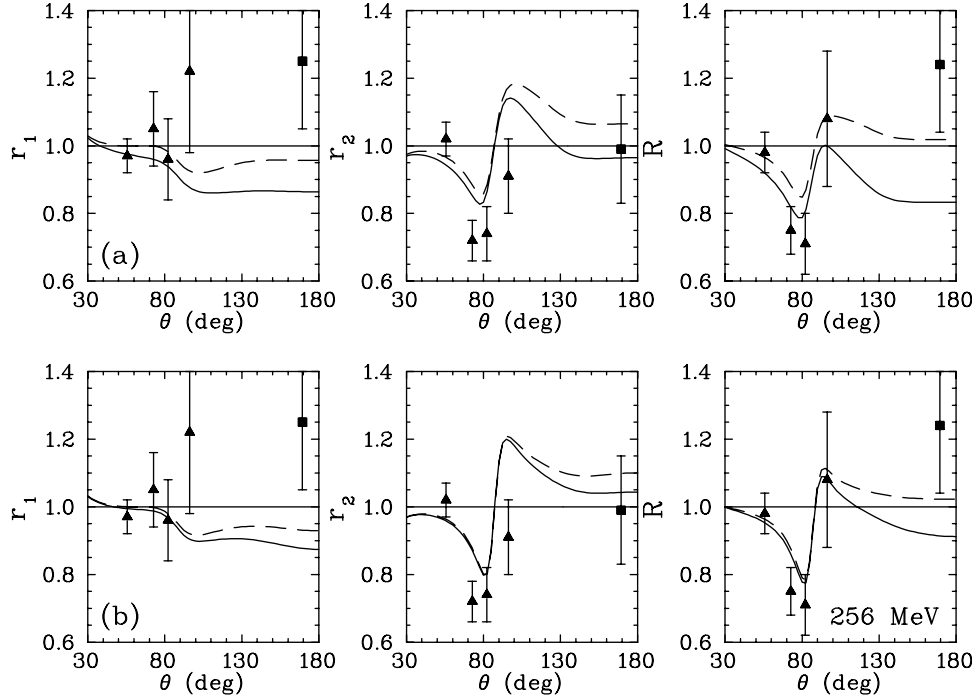


FIG. 14. The ratios  $r_1$  and  $r_2$  and the superratio  $R$  for  $T_\pi = 256$  MeV. The notation is the same as for Fig. 11.

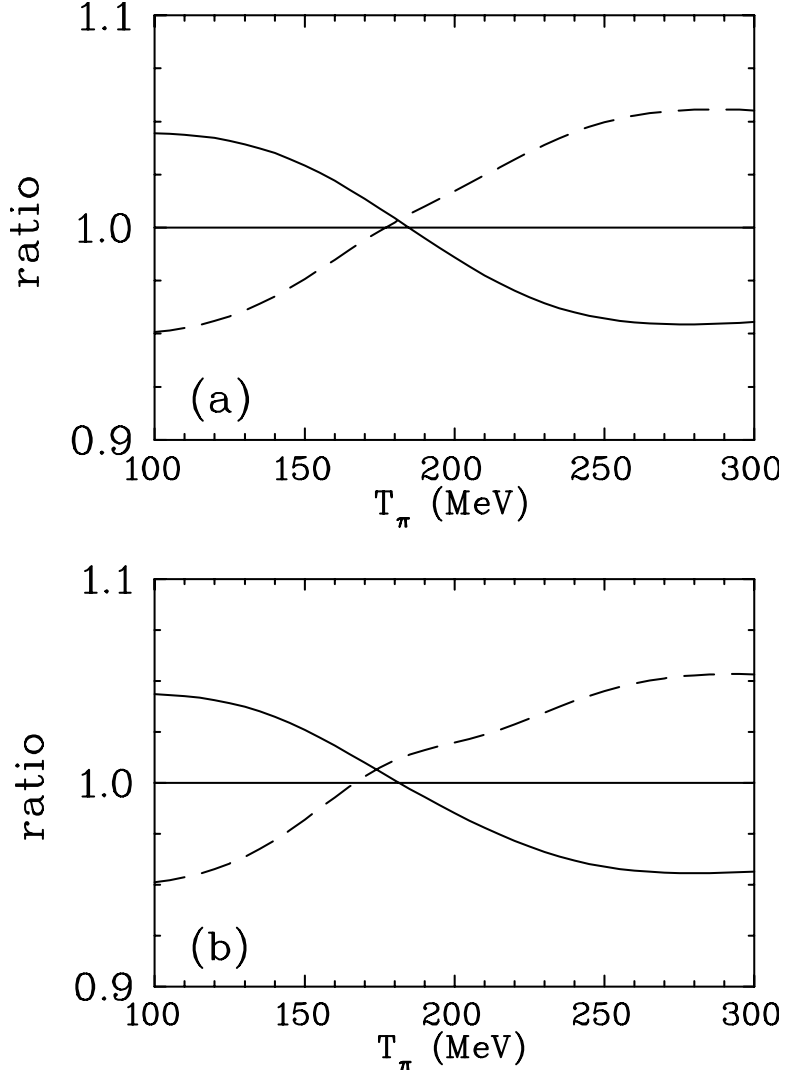


FIG. 15. Predictions for the ratios  $r_{1t}$  (solid), and  $r_{2t}$  (dashed) for the total  $\pi^{\pm 3}H/{}^3He$  cross sections. Calculations were done for single and double scattering with the  $\Delta_{33}$ -mass splitting. The Coulomb interactions are not taken into account. Plotted are the results for (a) WF (7) and (b) WF (8).

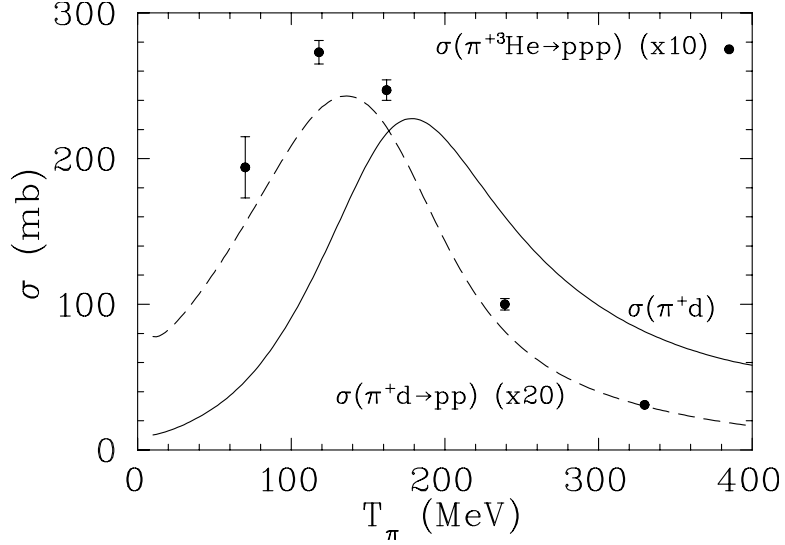


FIG. 16. Total  $\pi^+$  cross sections. Plotted are cross sections for  $\pi^+d$  (solid) and  $\pi^+d \rightarrow pp$  (multiplied by a factor of 20) (dashed) from a recent combined fit of the  $pp$  and  $\pi d$  elastic scattering with the  $\pi^+d \rightarrow pp$  data [32]. The  $\pi^3He$  absorption data (multiplied by a factor of 10) are from [33] (filled circles); it can be seen that they peak near  $T_\pi = 140$  MeV.